PROBE AND THERMOGRAPHIC MEASUREMENTS IN THE ASDEX DIVERTOR

U. Ditte, T. Grave

IPP III/102

December 1985

MAX-PLANCK-INSTITUT FÜR PLASMAPHYSIK

8046 GARCHING BEI MÜNCHEN

MAX-PLANCK-INSTITUT FÜR PLASMAPHYSIK

GARCHING BEI MÜNCHEN

PROBE AND THERMOGRAPHIC MEASUREMENTS IN THE ASDEX DIVERTOR

U. Ditte, T. Grave

IPP III/102 December 1985

Die nachstehende Arbeit wurde im Rahmen des Vertrages zwischen dem Max-Planck-Institut für Plasmaphysik und der Europäischen Atomgemeinschaft über die Zusammenarbeit auf dem Gebiete der Plasmaphysik durchgeführt.

Probe and Thermographic Measurements in the ASDEX Divertor

U. Ditte, T. Grave

Abstract

Measurements of plasma parameters in the divertor scrape-off, like temperature and density profiles and power flow onto the divertor plates, are presented for different main plasma conditions (OH-phase, L-phase, H-phase with bursts, H-phase without bursts, LH-current drive).

Statements about fast electrons, deviations from a Maxwellian electron distribution function and the electric potential in the scrape-off plasma are made. Comparison between probe measurements, microwave interferometry, Thomson scattering and measurements of the power flow onto the divertor plates are discussed.

Probe and Thermographic Measurements in the ASDEX Divertor

CONTENTS

IPP III/102 U. Ditte
T. Grave

PROBE AND THERMOGRAPHIC MEASUREMENTS IN THE ASDEX DIVERTOR

(December 1985)

1. Introduction

The best confinement and the cleanest discharges are obtained by divertor operation of the ASDEX tokamak. Application of the divertor results in low production and better retainment of impurities, especially with additional heating by neutral beam injection, and better plasma confinement (H regime) than in comparable limiter discharges.

To understand these desirable properties (touching questions of sputtering from the walls, particle and heat transport, etc.), one needs an exact knowledge of plasma parameters, such as the electron density, electron distribution function and electric potential in the divertor, and of the energy deposition on the neutralizer plates.

In this paper, we compare temperature and density profiles in the divertor measured by different methods (probes, microwave interferometry, Thomson scattering) for typical parameters of the main plasma and try to check their consistency.

Statements about fast electrons can be made by means of probe and energy deposition measurements. Combined with additional probe measurements, they allow conclusions about potentials in the divertor plasma and in the Debye sheath. We shall discuss whether the measurements of the energy flux onto the neutralizer plates are consistent with other plasma parameters close to the plates.

2. Arrangement of measuring systems

Figure 1 shows a basic drawing of the divertor. The magnetic flux lines in the OH-phase of the plasma are sketched. The solid line is the separatrix in the OH-phase, and the heavy, broken line labelled 'NI' designates the separatrix after switch-on of the neutral injection.

Figure 1 also shows the locations of the different electron density n_{ed} and electron temperature T_{ed} measurements in the divertor. The Langmuir double probe was used to measure n_{ed} and T_{ed} profiles at two positions: near the neutralizer plate ($z \approx 87$ cm) and at the exit of the divertor throat ($z \approx 75$ cm). An absolute calibration of the probe data was obtained by comparison of profile areas ($\int ndl$) measured along the direction where the line-integrated scrape-off density was measured with an 8.6 mm microwave interferometer. Laser scattering measurements were made along the vertical direction 4.8 cm from the neutralizer plate /1/. In addition to these diagnostics, the power deposited on the outer neutralizer plate was measured with an infrared camera.

3. Probe measurements in the divertor

3.1 Description of measuring apparatus

The probe measurements in the divertor were made with a double probe made of molybdenum (Fig. 2) which can be moved in two dimensions by means of a manipulator and a tilt mechanism. The cylindrical probe tips are aligned so that the plane defined by them is approximately normal to the magnetic field. The thermal load of the double probe is checked with thermocouples in the tips.

Characteristics are recorded by amplifying the sawtooth signal of a function generator (0-2 MHz) with a bipolar operational amplifier (± 72 V, ± 5A) and applying it to the probe during the tokamak discharge. The current and voltage signals of the double probe can be digitized at a maximum rate of 4 MHz, with 4000 measured points for each signal. In time intervals when the plasma parameters in the probe vicinity are approximately constant, the measured points of several characteristics can be superposed to improve the averaging process. Different methods of averaging are available. Within a given voltage interval, it is possible to obtain the appropriate average currents to generate a smooth characteristic. Additionally, a spline program can be used to create a fit through the measuring points according to the method of least squares. However, its application requires very much computer time.

It is also possible to use one of the probe tips as a single probe. In this case, the probe potential is floating in relation to the plasma, and only during a short time interval (0.1 ms - 100 ms) is it connected to the

vessel or the neutralizer plate via the sawtooth voltage source.

3.2 Probe theory

In the case of a Maxwellian plasma the current I of a double probe as a function of the probe voltage φ_p is determined by the system of equations (1) - (4), where i_{1e}, i_{2e} are the single probe electron currents and φ_1, φ_2 are the single probe potential differences between the probe and the plasma /2,3/:

$$I = i_{1e} - i_i = i_i - i_{2e}, \tag{1}$$

$$i_{1e} = I_{oe}\, e^{e\varphi_1/kT_e} \cdot G_e(\varphi_1), \tag{2}$$

$$i_{2e} = I_{oe}\, e^{e\varphi_2/kT_e} \cdot G_e(\varphi_2), \tag{3}$$

$$\varphi_p = \varphi_1 - \varphi_2. \tag{4}$$

The following abbreviations were used:

$$i_i = \left(e\sqrt{\frac{kT_e}{2\pi m_i}}\ nA\right) \cdot i_+ \cdot G_i \tag{5}$$

for the ion saturation currrent, and

$$I_{eo} = e\sqrt{\frac{kT_e}{2\pi m_e}}\ nA \tag{6}$$

for the thermal electron currrent, where A is double the cross-sectional area of the probe normal to the magnetic field, and i_+ is a factor calculated by Laframboise /4/ which depends on the probe potential and the ratio of the Debye length to the probe radius. The factors G_e and G_i take the influence of a probe shadow into account and depend on the particle transport in the shadow. G_e varies as the probe potential and describes the deviation of the electron characteristic from the exponential curve. G_i is smaller than unity and is independent of the probe potential.

The factor G_e reduces the slope of the double probe characteristic in the centre of symmetry, so that its influence has to be taken into account when the temperature is determined from this slope. With potentials far from the floating potential, the influence of G_e on the exponential growth of the

electron current is neglected. It is therefore possible to determine the electron temperature from the exponential growth of the electron current in this potential regime.

The density values can be calibrated by comparing a density profile measured with the probe with the corresponding line density obtained from microwave measurements (local dependences of the calibration factor being neglected). For ohmically heated plasmas and for the L and H phases of neutral injection this yielded

$$\int_{\mu\text{-wave}} n_{ed} \cdot dl = 1.78 \cdot \int_{\text{probe}} n_{ed}\,(G_e = 1,\ G_i = 1) \cdot dl, \qquad (7)$$

where $n_{ed}(G_e = 1, G_i = 1)$ means that $G_e = 1$ and $G_i = 1$ were assumed to calculate the density.

The presence of fast electrons may lead to alterations of the characteristics in the regimes of ion saturation current and incipient electron current. As an example, Fig. 3b shows the alteration of a characteristic caused by a group of monoenergetic electrons. Figure 3a depicts the same characteristic without this additional group of electrons. Local deviations in the distribution function and in the transport properties or electric fields in the plasma can cause a shift of the origin of axes for a double probe characteristic (Fig. 3c).

3.3 Measurements of density and temperature

The density and temperature profile measurements discussed in the following were taken shot by shot during the 'divertor series' of discharges 10804 to 10833 (Fig. 4). Additionally to the probe measurements, Thomson scattering and energy deposition data were taken.

Figure 5 shows the probe current I and the D_α emission signal resolved in time from t = 1 to t = 1.3 s. The three discharge phases OH, L, and H are clearly distinguishable in both the D_α and the probe signals. Figure 6 shows the probe current, the probe voltage and the D_α signal in the H phase. Obviously, bursts can lead to density breakdowns and density spikes.

Figure 7a shows measuring points obtained by superposition of several

double probe characteristics in the OH-phase.

Figure 7b shows the same characteristics after a smoothing procedure which averages over all current values within given voltage intervals. Such smoothed characteristics were taken for evaluation in the OH-phase. Figures 8a and 8b show superpositioning of several characteristics taken in the L and H-phases. For the L-phase, an average curve was fitted to the measuring points by eye and evaluated. For the H-phase, this procedure was repeated, but only for measuring points taken during the quiet phases. Bursts were not taken into consideration.

Figure 9 displays the radial profiles of density n_{ed}, electron temperature T_{ed} (determined from the slope in the centre of symmetry) and pressure $p_{ed} = n_{ed} \cdot T_{ed}$ measured with the Langmuir probe at the two positions indicated in Fig. 1. The results are for three distinct phases of the discharge: during ohmic heating (OH) and for the L and H-phases of neutral injection (P_{NI} = 3.1 MW). For comparison, the profiles measured along a chord at $z \approx 87$ cm are transformed along field lines to the position $z \approx 75$ cm. Differences in the two profiles of each plot are thus indicative of gradients in the divertor plasma parameters along the magnetic field. The feature common to all these profiles is a distinct peak near the separatrix and a broad shoulder on the large major radius side that extends out to the last flux surface passing through the divertor throat. The peak parameters for the OH and H-phases are very similar (note that the H-mode data shown here are for the quiescent period between H_α-spikes), whereas for the L-phase n_{ed} and T_{ed} are a factor of almost two higher. As far as gradients along B are concerned, the data would indicate the strongest effects inside the separatrix (for which there are no explanations at present).

Figure 10 Langmuir probe data are compared with results from Thomson scattering. (For this purpose the probe data were transformed along flux surfaces to the position of the laser scattering measurements; see Fig. 1.) For the OH-phase the densities measured by the two diagnostics agree very well, while the higher electron temperature measured by the probe could be explained by the effect of the magnetic field on these measurements.

For the H-phase, the two measurements were differently evaluated; the probe data are again for the quiescent periods between D_α-bursts, whereas the

laser scattering data are averages over quiescent periods and spikes. This could explain the shift in the peaks of the n_{ed} and T_{ed} profiles (which is in the direction of lower ß-values for the laser data). Most striking are the large differences in the absolute temperature obtained. This is due to the fact that in the H-phase the spectral profiles of scattered laser light (based on three spectral channels) cannot be fitted to a single temperature: the two outer channels, which contain most of the scattered light (they are therefore supposed to give the more relevant "temperature"), yield "temperatures" of 8 - 10 eV in the shoulder and a maximum of about 30 eV near the separatrix. The two central channels, on the other hand, yield "temperatures" between 1.5 and 4 eV.

Figure 11 shows the part of an OH-phase characteristic in which incipient electrons play a role. The incipient electron current I_e is filtered out by subtraction of the ion saturation current (straight solid line in Fig.11a). The curvature of the semi-logarithmically plotted incipient electron current (Fig. 11b) reflects the influence of the magnetic field on the characteristic. The slope of the tangent for probe voltages far from the floating potential gives another upper limit for the electron temperature (a pure exponential would give the real temperature provided the distribution function is Maxwellian /3/). In the case shown in Fig. 11b, the temperature obtained by the method discussed above is between 4.3 and 8 eV. Evaluation of the slope in the centre of symmetry yields 13.8 eV. Thus, we have reduced the influence of the magnetic field on the temperature measurement. Comparison of the three experimental methods - laser scattering, probe evaluation in the centre of symmetry of the characteristic, and probe evaluation by means of the incipient electron current - shows (Fig. 12) that the evaluation of incipient electron currents gives essentially the same results as the laser scattering experiments (regarding the respective error bars).

3.4 Fast electrons

To resolve the fine structure in the incipient electron part of the characteristic, a spline fit program was additionally employed. This program fits a spline function $\bar{y}(x)$ as smoothly as posible to the given measuring points $y_i(x_i)$ by the method of least squares /5/. The smoothness of the spline function can be varied by the smoothing parameter s. The spline function

satisfies the condition

$$\Sigma\ (\bar{y} - y_i)^2 \leq s \qquad (8)$$

for all measured points.

Figures (13a) - (13f) document the efficiency of the spline program. Figure (13a) presents values calculated by the following do-loop of a FORTRAN program to test the spline routine:

```
Do 10 I = 1,1000
x(I)    = I * 0.01-8.
10 y(I) = (exp x-1) * (1 + 0.3 * (cos(10 x)
          + cos (3x))) + 0.8 * cos (1000 x)
```

The term cos (1000 x) distributes the values statistically owing to its fast oscillation. Figure (13b) shows the function

$$y = (e^x-1) * (1 + 0.3 * (\cos 10x + \cos 3x))$$

contained in Fig. (13a). Figure (13c) is a plot of the function

$$y = e^x-1,$$

also contained in Fig. (13a).

Figures (13d) - (13f) present spline fits through the points of Fig. (13a) for different smoothing parameters s. Figure (13d) with a smoothing parameter of 250 looks very similar to Fig. (13b) but shows additional small-amplitude oscillations. Increasing the smoothing parameter to s = 302.5 causes these oscillations to vanish: the resulting curve (13e) shows approximately the same shape as (13b). A further increase of s to 624 smoothes the remaining oscillations and yields curve (13f), which reproduces (13c) very well except for a small part at the extreme left. Thus, the spline program is able to discover structures deliberately superimposed by statistically distributed points.

If the spline program is applied to probe characteristics measured during the OH-phase, a systematic increase of the smoothing parameter leads to

different shapes of the ion saturation part of the curves near and 2 - 3 cm beyond the separatrix (Figs. (14) - (17)). The curve measured near the separatrix (Figs. (14c), (15c)) can be interpreted as a superpositioning of a smooth ion saturation current (broken extrapolation) and an additional component of non-thermalized electrons (shaded area).

For the same discharge, Figs. (14a) - (14c) and (15a) - (15c) show the ion attracting part of the characteristic for the upper and the lower tip of the double probe, respectively. For both tips, hot electrons are detected in the same voltage range ($\varphi_p > 35$ V).

In the shoulders of the profiles beyond the separatrix (Fig. 9), fast electrons in the ion saturation part of the characteristic cannot be resolved (Fig. 16d).

Owing to the unsatisfactory statistics in the L-phase it is not quite clear if the deviations in the saturation part of the characteristic are also caused by fast electrons (Fig. 17). Their potential contributions are indicated by the shaded areas. The tilting of the curve at its extreme ends is explained by the bad statistics (analogous to Fig. 13f).

The flux of fast electrons can now be evaluated from the probe data to approximately 1.5×10^{18} cm^{-2} s^{-1} in the OH-phase. The following equation allows estimation of the possible flux of plasma across the separatrix into the divertor

$$j_{\parallel} = \frac{A_s}{A_{\parallel} \cdot \sin\theta} D_s \cdot \left.\frac{dn_{em}}{dr}\right|_s \cdot \qquad (9)$$

A_s is the plasma surface at the separatrix, $A_{\parallel}$ the flow-off area for fast electrons in the divertor and θ the tilting of the magnetic field lines. With $D_s = 4000$ cm^2/s, $(d\, n_{em}/dr)/_s = 3 \times 10^{12}$ cm^{-4} /6/, eq. (9) yields a possible flux of fast electrons of 1.1×10^{19} cm^{-2} s^{-1}, which could be detected by the probe. If you consider that this flux is subject to recycling losses, the measurement of the flux in the divertor appears to be consistent with our knowledge of diffusion coefficients and density gradients in the plasma midplane. In the given situation, electrons in the midplane are measured to be distributed according to a Maxwellian up to

energies of 700 eV /6/. For comparison, it might therefore be informative to calculate the possible collision-free flux into the divertor

$$j_{\perp} = n_{em} \frac{\int_{e}^{\infty} - \frac{mv^2}{2kT_{em}} v \, dv}{\int_{-\infty}^{\infty} - \frac{mv^2}{2kT_{em}} dv} = n_{em} \sqrt{\frac{kT_{em}}{2\pi m_e}} \; e^{- \frac{mv_o^2}{2kT_{em}}} . \qquad (10)$$

Electrons can reach the divertor without collisions if their energy exceeds 150 eV (see also 4.3.1). For the given midplane parameters (T_{em} = 80 eV(OH), n_{em} = 8 x 10^{12} cm^{-3} (OH) /6/), eq. (10) yields a flux of 1.8 x 10^{20} cm^{-2} s^{-1}. The discrepancy between the possible diffusive plasma flux across the separatrix - consistent with the probe data in the divertor - and the possible collision-free flux from the tail of the Maxwellian in the midplane provides evidence that an electron-retarding potential of about $-4.7\,kT_e$ is established between midplane and divertor plates. For the L and the H-phases during neutral injection, the situation seems to be similar.

3.5 Plasma potentials

In the preceding section we already pointed out that the electrons running away collisionlessly from the ions in the midplane are retarded by a potential. We shall now discuss what local distribution of the potential is to be expected between the midplane and divertor plates.

In the divertor, single-probe characteristics were taken with the neutralizer plate acting as a reference probe. If one compares the floating potential of the single probe measured outside the separatrix at the edge of the profile shoulder (Fig. 18) with the floating potential of the neutralizer plates, differences of only a few volts are found. The plasma potential derived from the characteristics of Fig. 18 is below 15 V. Hence, it can be concluded that there is no potential drop of a few hundred volts along flux lines between the probe position and the plate. Near the separatix, a high potential drop to the plates is only possible if the same drop also exists radially. A large radial drop would considerably shift the origin of the double probe characteristics, which was not observed.

Charging of the Debye sheath and plasma in front of the plate outside the probe range to values as high as a few 100 eV can therefore be excluded. Charging of the plasma along flux lines in the range of the probes can also be excluded since only weak gradients of the electron pressure were measured.

The probe data are consistent with simple models for the Debye sheath and the plasma presheath. The potential drop φ_w across the Debye sheath can be estimated from the condition that there is no electric current from the plasma to a plate in contact with this plasma. A graphical solution of the equation (see Fig. 19)

$$0.5 \cdot \sqrt{\frac{kT_e}{m_i}}\,(n + \varepsilon) = \sqrt{\frac{kT_e}{2\pi m_e}}\; n \cdot e^{-\varphi_w/kT_e} + \varepsilon \sqrt{\frac{kT_h}{2\pi m_e}}\; e^{-\varphi_w/kT_h}\,, \tag{11}$$

where T_e and n are the temperature and density of the cold electrons, and T_h and ε are the temperature and density of the hot electrons, respectively, shows that charging of the plates via the Debye sheath to potentials exceeding $3kT_e$ requires hot electron fluxes of

$$\varepsilon \sqrt{T_h} > 0.035 \cdot n \sqrt{T_e}\,. \tag{12}$$

Such large fluxes of hot electrons are not observed in the divertor.

A different model based on a paper by Harrison and Thomson /7/ allows investigation of plasma charging by hot electrons. Consider a plasma between two walls (Fig. 20). The plasma consists of electrons and cold ions permanently generated in the bulk of the plasma for reasons of stationarity. After their generation, the ions are collisionless. On the assumption of quasi-neutrality ($L \gg \lambda_D$)

$$n_e = n_i \tag{13}$$

the following equation for the plasma potential is yielded:

$$n\, e^{-\eta} + \varepsilon\, e^{-T_e/T_h\,\eta} = \left(\frac{M}{2kT_e}\right)^{1/2} \int_0^{\eta} g(\eta_\xi)\,(\eta-\eta_\xi)^{-1/2}\,\frac{d\xi}{d\eta_\xi}\,d\eta_\xi\,, \qquad (14)$$

where

$$\eta = -\frac{e\varphi}{kT_e} \qquad (15)$$

and $g(\xi)d\xi$ is the number of ions generated per second in the interval ξ, $\xi + d\xi$. Inversion of eq. (14) and the condition $d\xi/d\eta = 0$ (formation of the space charge layer) produce the equation for the potential η_1 at the edge of the space charge layer:

$$0 = [\eta_1^{-\frac{1}{2}} - 2\, e^{-\eta_1}\, D(\sqrt{\eta_1})] + \frac{\varepsilon}{n}\sqrt{\frac{T_e}{T_h}}\,\cdot$$
$$[\left(\frac{T_e}{T_h}\,\eta_1\right)^{-\frac{1}{2}} - 2\, e^{-T_e/T_h\,\eta_1}\cdot D(\sqrt{\frac{T_e}{T_h}\cdot\eta_1})], \qquad (16)$$

where D(x) is the Dawson function $D(x) = \int_0^x e^{t^2}\,dt$.

Typical solutions of eq. (16) are shown in Fig. 21. The potentials at the intersections of the broken and solid curves represent the plasma potentials at the sheath edge. Below a critical concentration $\frac{\varepsilon}{n}$, the solution of eq. (16) is not unique owing to the three extrema in the curve $\xi(\eta)$. As discussed in the following, the unique and non-unique solutions just separate the regimes of charged and non-charged plasma. Potentials at the sheath edge so obtained are independent of the source function $g(\xi)$.

An exact solution of eq. (14) exists if one assumes that the ion generation is independent of the location in the plasma volume, i.e. if

$$g(\xi) = g_o. \qquad (17)$$

In this case

$$s = e^{-\eta} D(\sqrt{\eta}) + \frac{\sqrt{T_h}\,\varepsilon}{\sqrt{T_e}\,\eta}\, e^{-\frac{T_e}{T_h}\eta} \cdot D\left(\sqrt{\frac{T_e}{T_h}\cdot\eta}\right) \cdot \qquad (18)$$

Here, we have introduced the normalized coordinate

$$S = \frac{g_o \cdot \xi}{\left(\frac{2kT_e}{M}\right)^{1/2}_n} \cdot \frac{\pi}{2} \cdot \qquad (19)$$

In Fig. (22), the plasma potential is plotted as a function of the coordinate s for $T_e/T_h = 0.01$. For small concentrations of hot electrons (1 %), the solution behaves as in the case $\varepsilon = 0$. Only for higher concentrations does the function $s(\eta)$ show a second maximum, but the sheath solution is still obtained with low sheath potentials ($\eta_1 \approx 1$), so that the plasma is still not charged. For high concentrations of hot electrons ($\varepsilon/n \geq 0.35$), the solution switches to high wall potentials ($\eta_1 \approx 85$). One can clearly see: charging of the plasma by fast electrons in stationary equilibrium is only possible with very high concentrations of fast electrons.

If one extends the essential result of the model to the situation in the divertor, one has to expect charging of the divertor plasma only at locations where many hot electrons may be present. However, only small concentrations of hot electrons are measured after the plasma has penetrated through the divertor throat. Hence, a charging of the divertor plasma in the area between throat and plates can be excluded.

Measurements in the midplane show that the plasma edge is positively charged ($e\varphi(r) > kT_{em}(r)$) in this region (see Fig. 23).

Roughly, the potential distribution between midplane and plates results as plotted in Fig. 24. From the midplane to the exit from the divertor throat, the plasma is charged to a potential of approximately 5 kT_{em} (see also Sec. 4.3.2). Owing to the subsequent enhancement of density ($n_1 \ll n_2$), a

potential minimum is expected above the throat. Along the further course of the flux lines, the potential is constant except for the close vicinity of the neutralizer plates. In the Debye sheath in front of the plates, the potential drops by an additional 3 kT_{ed}.

The mechanism that establishes these high potentials (5 kT_{em}) between the midplane and divertor plates is not yet clear. A double sheath could provide such a mechanism /8/. It is also possible that the profiles measured at the midplane have to be shifted inwards owing to the insufficient knowledge of the true position of the separatrix /6/. Thus, lower temperatures than assumed above might be present at the separatrix, thus eliminating the reasons for a high potential.

3.6 Deviations from a Maxwellian

Except for a small fraction of fast electrons, there is no evidence for deviations from a Maxwellian in the OH-phase. In the L and H-phases, the characteristics measured near the separatrix exhibit displacements of their respective origins. Electric fields perpendicular to the profile (Fig. 9) are not very likely to provide a reason for these displacements because their sign can change with time (measured in the flank of a profile). Locally varying transport properties are not very likely either, since the probe profile shape coincides with the results of the laser scattering measurements even during the neutral injection phase if you assume a locally uniform scaling factor for the density. On the other hand, the laser scattering measurements have shown that the distribution function of the electrons is non-Maxwellian in the H-phase and the bulk part of the particles has a temperature of 30 eV. Since the probe measurements yield considerably lower temperatures, the displacements of the origin are attributed to non-Maxwellian distribution functions which are locally different. Figure 25 shows a characteristic taken during the OH-phase which shows no displacement, and a characteristic taken during the L-phase of the same shot. The shift amounts to about 15 V.

Possibly, the non-Maxwellian behaviour is caused by the proximity of the wall. The mean free path for 30 eV electrons in the divertor is about 0.5 m, and the wall is approximately 1.0 m away from the probe position. Thus, the distance between probe and wall and the mean free path are quite comparable, and discrepancies between simple models and experimental

observations are not too surprising. Additionally, the character of the profile leads to the expectation that the wall is charged to some average floating potential, and electrons are therefore preferably lost close to the separatrix.

3.7 Profiles during burst-free H-phases

Figure 26 shows the plasma current, density and D_α radiation of a discharge series with burst-free H-phases. For selected time intervals, density and temperature profiles are sketched in Fig. 27. The profiles were taken at the position $z \approx 80$ cm. Temperatures were determined by evaluation of the gradient at the centre of the characteristics.

3.8 Profiles during LH current drive

Figure 28 shows plasma current and density for a series with LH current drive. During the lower hybrid pulse the plasma current was purely sustained by current drive. Profiles measured during the OH-phase and during LH current drive are shown in Fig. 29. The temperature in front of the neutralizer plates rises by a factor of about two, while the density is lowered by the same factor. The decrease of the density is consistent with microwave measurements in the divertor showing a lowering of the line density by about the same factor of two.

4. Measurement of the energy flux onto the neutralizer plates

4.1 Measuring apparatus

The surface temperature of the neutralizer plate in the outer, upper divertor chamber of the ASDEX tokamak is measured by the infrared thermography system described in Ref. /9/. A TV camera sensitive in the wavelength interval 3 - 5 µm is placed outside the vacuum vessel and views the thermal radiation emitted by the neutralizer plate through an infrared optical system and a CaF_2 window in the vessel wall. The plate is made of titanium and extends over 18 cm in the vertical direction (between coordinates z = 80.4 and 98.4 cm). Its surface temperature $T_S(z)$ is scanned along this direction every 400 µs. A scan consists of 128 individual measuring points

which corresponds to a spatial resolution of about 1.5 mm. The camera signal is digitized by a 12 bit A/D converter and enters a buffer memory, from which a PDP - 11/34 computer transfers it to its final storage medium, a magnetic tape or disc.

The camera output was calibrated in the following way. Firstly, we focussed the camera on a black body of known temperature and recorded the camera signal over a range from about 15 to 220° C. Then we scanned the neutralizer plate with the camera and compared the signal strength with the signal produced by the black body at the same temperature. The IR emissivity of the Ti plate turned out to be about 54 % of that of a black body and to be uniform to within 15 % over the whole width of the plate. Thus, calibrated measurements of the surface temperature are possible up to temperatures of about 400° C if one assumes an emissivity constant with temperature.

4.2. Method of evaluation

The energy fluxes deposited on the wall are computed from the temporal evolution of the surface temperature profiles according to the method developed by B.K. Bein. We do not intend here to give an elaborate survey of the theory involved in the calculations but only want to sketch the essential ideas (for details, see Refs. /9,10/). The calculation is one-dimensional, i.e. it does not assume heat flow parallel to the surface of the neutralizer plates but only perpendicular to it. This means that any temperature rise at a particular measuring point in the profile is treated as being caused by some energy flow from the plasma to the plate though in reality it could be caused by diffusion. The equation to be solved for each measuring point is the one-dimensional heat conduction equation

$$\frac{\partial T_w(z,y,t)}{\partial t} = \kappa \frac{\partial^2 T_w(z,y,t)}{\partial y^2} , \qquad (20)$$

where T_W is the temperature inside the wall, y the coordinate perpendicular to the surface, and κ the thermal diffusivity of the wall material. The measured quantity is, of course,

$$T_s(z,t) = T_w(z,\ y \to 0,t) \qquad (21)$$

and the quantity of interest, the energy flux to the surface, is given by

$$Q_s(z,t) = -K \left[\frac{\partial T_w(z,y,t)}{\partial y}\right]_{y \to 0} . \qquad (22)$$

K is the thermal conductivity and is connected to the diffusivity via $\kappa = k/\varrho c$, where ϱ is the mass density and c the specific heat. Equation (20) is solved for the temperature distribution inside the plate under the boundary condition that there be no power loss at the plate's rear surface at y = 0.2 cm, i.e. that $-K\partial T_w(z, y \to 0.2\ \text{cm}, t)/dy = 0$. For the rather lengthy expressions for the temperature distribution and the energy flux inside the plate the reader may refer to /9/. Owing to the problems with possible divergence of the solution for the energy flux at y = 0, the expression for Q(z,y,t) is expanded in a Taylor series in terms of $y - y_o$, where y_o is an appropriately chosen location slightly inside the bulk of the wall. This new expression converges for $y \to 0$ and can be evaluated by numerical computation. As a by-product, the calculation yields the rear surface temperature of the plate (not accessible to the measurement) as a control over the heat diffusion time scale. Provided the thermal properties of the plate material are isotropic, the calculated rear temperature rise caused by some energy flux onto the front surface at location z is expected to be equal to the temperature rise at $z \pm 0.2$ cm caused by heat propagation parallel to the surface. So the magnitude of the calculated rear surface gives a measure of profile broadening by diffusion effects, which were neglected in our one-dimensional treatment.

Typically, after an ohmically heated discharge with 2 s of approximately constant energy flow to the plates, the increase of the rear temperature is calculated to reach about 30 to 40 % of the surface temperature increase. Thus, for $t \gg 1$ s in OH-discharges, measured energy flux profiles have to be judged with some care because they may be broadened by diffusion effects. For this reason, we did not evaluate energy fluxes in these late phases of OH-discharges. For neutral injection phases, the period of increased energy flux to the plate is so short that profile broadening due to diffusion is not expected for the complete phase of additional heating (i.e. the calculated increase in rear temperature is negligible compared with the front temperature increase for any time in an L or H-phase). For the reasons discussed above, the development of a two-dimensional computer code for the evaluation of surface temperature profiles does not appear to be an urgent issue.

4.3. Results of measurements and comparison with other diagnostics

4.3.1 Methods of comparison

To correlate density and temperature profiles of the plasma in the divertor chamber measured by probes to the energy flux profiles onto the plate, it is necessary to 'project' the probe measuring points at radial positions R in the proper way onto the plate, i.e. along magnetic flux surfaces. Numerical calculations of the plasma equilibrium position /11/ were employed to get the correct curvature of the scrape-off layer during particular phases of the discharge. This curvature, and hence the location of the intersection point of the separatrix with the plate, may vary with time due to variations in the vertical field component which are controlled by a feedback circuit.

To calculate the energy flux Q_s to the surface as a function of the divertor plasma density n_{ed} and temperature T_{ed} for a given location R in the scrape-off profile, we used the equation

$$Q_s(Z,t = F(R,t) \cdot [\{(1-R_E)\cdot(\frac{M_i}{2} C_s^2(r,t) + \frac{\gamma}{\gamma-1} k\, T_{ed}(R,t) + 2.8\, k \cdot T_{ed}(R,t) + 13.6\ eV\} + 2\, k\, T_{ed}(R,t)] \cdot \sin\theta, \quad (23)$$

where F is the particle flux

$$F(R,t) = n_{ed}(R,t)\, c_S \quad (24)$$

and c_S the speed of sound

$$c_S = 2k\, T_{ed}/M_i, \quad (25)$$

where M_i is the mass of the plasma ions. Correlation between radial positions R and vertical positions z is achieved by the projection method cited above. Equation (23) reflects the following physical assumptions: energy is transferred from the plasma to the wall surface by ions (first term of the sum in square brackets) and electrons (second term). The energy transfer from ions to the wall is subject to a reflection coefficient R_E, which is assumed to be approximately 0.5 for the temperature range of

interest (0...10 eV) /12/. We want to stress that this value is only some reasonable low-energy extrapolation of experimental data taken with particles of far higher incident energy. The ion energy consists of several parts: kinetic energy $(M_i/2)\cdot c_s^2$, convective energy $[\gamma/(\gamma - 1)] \cdot kT_{ed}$ ($\gamma = 5/3$ is the ratio of specific heats), and a part ($2.8\ kT_{ed}$) which is picked up from the electrons on their path through the electrostatic sheath in front of the plate. Since all ions are neutralized by their contact to the wall, we assume an additional transfer of the ionization energy (13.6 eV) to the surface which is not subject to the energy reflection coefficient. Recombination of the atoms to deuterium molecules could further add an amount of about 2.2 eV per atom to the wall, but since we do not know the fraction of atoms recombining, and the amount of energy released is quite small, we do not include the effect in eq. (23).

When electrons enter the electrostatic sheath, they carry an energy of $4.8\ kT_{ed}$, of which $2.8\ kT_{ed}$ is transferred to the ions and $2\ kT_{ed}$ is brought to the wall by the electrons themselves. The term $\sin\theta$ takes into account that the scrape-off layer and wall enclose an angle of approximately 3.2° which reduces the energy flux onto the plate to about 1/18 of that through a plane intersecting the scrape-off layer perpendicularly.

4.3.2. Discussion of measured profiles for OH, L, and H-phases

Figures 30 and 31 show measured energy fluxes in the OH-phase of a double-null divertor discharge (I_p = 320 kA, $n_{ed} = 3.6 \times 10^{13}\ cm^{-3}$, P_{NI} = 3.1 MW), compared with calculations from temperature and density profiles according to eq. (23). For Fig. 30, the profiles were recorded with Langmuir probes, T_{ed} being determined from the slope in the centre of symmetry, for Fig. 31 by Nd-YAG laser scattering. In the OH-phase, the energy fluxes calculated from these probe data are far larger than the measured ones. A possible reason for this discrepancy could be the existence of temperature and density gradients between the probe measuring points and wall surface. At the left-hand side of the probe profiles, the distance of the particles to the plate along magnetic flux surfaces is only some tens of centimetres (18 cm for the innermost profile point) while - owing to the grazing angle of incidence - particles at the extreme right-hand side have to cover a distance of about 2.5 m before contacting the wall. The combined SOLID/DEGAS numerical scrape-off simulation codes /13,14/ predict a

monotonous decrease of the temperature towards the plate owing to the influence of recycling, and a maximum in density typically between 1 and 2 m from the wall. Thus, for most probe profile points the plasma density is expected to be higher than at the corresponding profile point on the plate. For a given probe measuring point, i.e. a given distance to the plate along flux lines, n_{ed} and T_{ed} were therefore corrected by a factor corresponding to the numerically calculated variation over this distance. Calculations of the energy flux using these 'corrected' values of n_{ed} and T_{ed} are also shown in Figs. 30 and 31. In the case where the probe data were used, the corrected energy flux is still higher than the measured one. As already mentioned earlier (Sec. 3.3), the temperatures measured with probes are impaired by a systematic error caused by the influence of the magnetic field on the probe characteristics. It is possible to avoid this interfering influence by obtaining the temperature not from the conventinal evaluation of the characteristic's slope near zero potential but from the curvature of the incipient electron current. This makes the temperatures very similar to results obtained from laser scattering experiments (Fig. 12). Figure 31 shows energy flux profiles calculated from laser scattering measurements of the temperature and density in the OH-phase compared with the measured energy flux. The agreement is better than with the probe data where T_{ed} is determined from the slope in the centre of symmetry. However, the calculated profiles from both probe and laser measurements show half-widths about twice as large as the energy flux profiles obtained from thermography (calculated half-widths: 2.5...3 cm, experimental: <1.5 cm). A candidate possibly responsible for this discrepancy might be a structure in the energy dependence of the reflection coefficient R_E for energies below 10 eV /15,16/. Thus, for the OH-phase, it can be concluded that probe, laser scattering and thermography measurements are not necessarily in contradiction to each other.

For the L-phase, the situation is different. Figure 32 shows that the measured energy flux is a factor of at least two larger than calculated from Langmuir probe data. The possibilities for misinterpretation of the probe data discussed above, especially the questionable evaluation of the temperature from the slope near the centre of the characteristics, could only produce an even smaller result for the calculated energy flux. Again, the measured profile width (FWHM < 1 cm) is a factor of about two smaller than that calculated. Hence, for the L-phase, the plasma in the divertor chamber in front of the plates cannot be responsible for the observed energy flux. The need for an additional physical mechanism not discussed so far is evident.

A candidate for this process might be energy transport by high-energy particles originating from the scrape-off layer in front of the main plasma. The average distance from the plates to the equatorial plane along flux surfaces is about 15 m. At the separatrix in the midplane, plasma temperatures T_{em} of 80 eV in the OH-phase and over 100 eV in the L and H-phases were determined by ruby laser Thomson scattering /6,17/. Certainly, some particles in the high-energy tails of the distribution functions attached to these temperatures may penetrate to the plates without losing energy by collisions. The minimum velocity for particles to attain a free path of length λ (15 m in our case) is

$$V_{min} = \lambda/\tau \ . \qquad (26)$$

This minimum velocity determines the minimum energy which must be possessed by the particles to travel without collisions over the distance of about 15 m from the midplane to the divertor plates:

$$\frac{1}{2} m V_{min}^2 = \sqrt{\frac{e^4}{4\pi \varepsilon_o^2} n_{em} \cdot \lambda \cdot \ln\Lambda} \ . \qquad (27)$$

n_{em} is the plasma density at the separatrix at the midplane, and $\ln\Lambda$ denotes the Coulomb logarithm. For typical midplane parameters (n_{em} = 6...8 x 10^{18} m^{-3}, $\ln\Lambda$ = 7...8) one gets

$$1/2\ mV_{min}^2 = 135 \ldots 150 \text{ eV}. \qquad (28)$$

In the following calculation we shall use E_{Min} = 150 eV.

For the estimation of plate potentials, particle fluxes and energy fluxes to the neutralizer plates, we describe the particles at the midplane by a Maxwellian truncated at the minimum velocity:

$$f_{i,e}(V_x, V_y, V_z) = \left(\frac{m_{i,e}}{2\pi k\, T_{em}}\right)^{3/2} \theta(V_z - V_{zmin})\, e^{-\frac{m_{i,e}(V_x^2 + V_y^2 + V_z^2)}{2\,k\,T_{em}}} \quad . \quad (29)$$

V_z is the component of the particle velocity parallel to the magnetic field, and θ is the Heaviside step function. The energy parallel to the field is conserved:

$$1/2\ m_i\ V_{iz}'^2 = 1/2\ m_i\ V_{iz}^2 - e\varphi_w,$$

$$1/2\ m_e\ V_{ez}'^2 = 1/2\ m_e\ V_{ez}^2 + e\varphi_w.$$

V_z' is the velocity in front of the neutralizer plate. Here, a potential will be produced which retards fast electrons and accelerates ions in a way that the resulting electron and ion fluxes to the wall are equal and the plasma does not lose net charge:

$$F_{fe} + F_e = F_{fi} + F_i \quad . \quad (30)$$

Indices fe and fi denote fast electrons and ions, respectively. Thermal particles in the divertor chamber that are small in energy compared with the fast ones are labelled e and i. We assume that hot and cold particle components penetrate each other and do not separate as in the case of a double sheath /8/.

For efficient retardation of fast electrons, $|\varphi_w|$ will turn out to be so large that the flux of 'cold' electrons F_e is negligible, and eq. (30) reads

$$\sqrt{\frac{k\,T_{em}}{2\pi\,m_e}} \cdot n_{em} \cdot e^{e\varphi_w/k\,T_{em}} \sin\theta = [(1-L_{cx}) - \sqrt{\frac{k\,T_{em}}{2\pi\,m_i}}\, n_{em} \cdot e^{-\frac{m_i\,V_{min}^2}{2k\,T_{em}}} + \sqrt{\frac{k\,T_{ed}}{2\pi\,m_i}}\, n_{ed}] \cdot \sin\theta \quad . \quad (31)$$

The potential is then given by

$$\frac{e\varphi_w}{k\,T_{em}} = \ln\left[\left(\frac{m_e}{m_i}\right)^{\frac{1}{2}} ((1-L_{cx}) \cdot e^{-\frac{m_i \cdot V_{min}^2}{2k\,T_{em}}} + \frac{\sqrt{T_{ed}}\, n_{ed}}{\sqrt{T_{em}}\, n_{em}})\right]. \quad (32)$$

Table 1

Phase	n_{em} ($10^{12}cm^{-3}$)	T_{em} (eV)	n_{ed} ($10^{12}cm^{-3}$)	T_{ed} (eV)	Q_s ($\frac{W}{cm^2}$)	Q_{Fe} ($\frac{W}{cm^2}$)	Q_{fi} ($\frac{W}{cm^2}$)	Q_i ($\frac{W}{cm^2}$)	F_{fe} ($10^{17}cm^{-2}s^{-1}$)	F_{fi} ($10^{17}cm^{-2}s^{-1}$)	F_i ($10^{17}cm^{-2}s^{-1}$)	$\mathcal{F}_{fe}$ ($10^{21}s^{-1}$)	φ_w (kT_e)
OH	8	80	26	5	25	19	0.08	21.5	7.7	0.15	7.5	1.5	-4.4
L	6	130	40	22	145	108	1.9	92	26	0.31	26	5.2	-3.1
H (between bursts)	6	250	26	10	20-45	104	9.7	101	13	0.71	12	2.6	-4.13

n_{em}: plasma density averaged over total scrape-off length
T_{em}: plasma temperature at separatrix at midplane
n_{ed}: plasma density in the divertor (for explanation, refer to text)
T_{ed}: divertor temperature
Q_s: total measured energy flux to a single divertor plate
Q_{fe}: fraction carried by fast electrons
Q_f: fraction carried by fast ions
Q_i: fraction carried by thermal divertor ions
F_{fe}: flux of fast electrons to a single plate
F_{fi}: flux of fast ions to a single plate
F_i: flux of thermal divertor ions to a single plate
$\mathcal{F}_{fe}$: calculated total fast electron flux to an outer plate (circumference 10 m, profile width 1 cm)
φ_w: sheath potential

L_{CX} is a charge exchange loss factor which takes into account the fact that only a small fraction of fast ions will penetrate the divertor chamber without being neutralized. $L_{CX} = 0.9$ might be a realistic choice. This means that the flux of fast ions to the wall is small compared with F_i (the flux of thermal divertor ions), but since these few fast ions may carry a considerable amount of energy, we shall not drop this term.

For the energy flux onto the plates, one obtains

$$Q_s = [2k \cdot T_{em} \sqrt{\frac{k\,T_{em}}{2\pi\,m_e}} \cdot e^{e\varphi_w / k\,T_{em}} \cdot n_{em} + (1-R_E)\,((1-L_{cx}) \cdot (2k\,T_{em} - e\varphi_w + \tfrac{1}{2}\,mV^2_{min}) \sqrt{\frac{kT_{em}}{2\pi\,m_i}} \cdot e^{-\frac{mV^2_{min}}{2k\,T_{em}}} n_{em} + (2k\,T_{ed} - e\varphi_w) \cdot \sqrt{\frac{kT_{ed}}{2\pi\,m_i}} \cdot n_{ed})] \cdot \sin\theta \qquad (33)$$

Of course, R_E might be different for high and low-energy particles, but is considered constant for our order-of-magnitude estimation. The results of the calculation are compiled in Tab. 1.
For the interpretation of Tab. 1, a remark should be made concerning the scrape-off density of 'cold' ions in the divertor, n_{ed}. For the OH-phase, $n_{ed} = 1.3 \times 10^{13}$ cm^{-3} would be a realistic value, with a profile width of about 2...3 cm. The flux of fast electrons has a width of only about 1 cm, but since we assume that ions originating from the total 'cold' ion profile width balance the flux of the fast electrons, we inserted the ion density times the profile width into eq. (30), and thus this integrated value also enters Table 1.

In the OH and L-phases, measured and calculated energy fluxes differ only by a factor of two. In the H-phase, the calculated fluxes are larger than the measured ones by a factor of ten. Though our model reduces the energy fluxes, it is not able to describe the situation from midplane to divertor quantitatively correctly. In the model, we have assumed that both plasmas penetrate each other, and that the sheath forms in front of the neutralizer plate. The probe measurements have shown that the plate is not charged to a few kT_{em}. If at all, the formation of the electron-retarding potential takes place in front of the divertor plasma. In this case, the energy flux to the plates is only determined by hot electrons from the midplane, which

can penetrate the potential barrier, and by cold electrons and ions in the divertor, which are only subject to a very small potential. The energy flux of the hot ions is negligible owing to the CX losses. Because the energy flux is essentially only converted on its way from the midplane to the divertor, a rather exact measure of the potential is given by

$$\frac{e\varphi_w}{k\,T_{em}} = \ln\left[\frac{Q_s}{2k\,T_{em}\sqrt{\frac{kT_{em}}{2\pi m_e}}\,n_{em}\cdot\sin\theta}\right] . \qquad (34)$$

If one inserts the measured energy flux to the plates for Q_s, and for T_{em} and n_{em} quantities measured in the midplane, the resulting φ_w gives the potential that retards the energy flux from the midplane. Energy fluxes sustained by ions are neglected. Radiation losses lead to a mistake by a factor of two in the energy flux which means that $e\varphi_w/kT_{em}$ is determined to within +0.7. For the OH-phase, $e\varphi_w/kT_{em}$ = -5.4 is yielded, for the L-phase -2.1, and for the H-phase -5.3 (between bursts).

As in Sec. 3.4, high potentials between the divertor and midplane are deduced.

4.3.3 Discussion of measured profiles in the H-phase

For the H-phase, we have to discriminate between two different cases: H-phases with numerous outbursts of ELM's, or H-phases with long quiet periods without burst activity.

- H-phases with high burst frequency

  Figure 33 shows the D_α line emission intensity during the neutral injection phase of an ASDEX discharge with high burst frequency (about 20 bursts in 120 ms). Each burst indicates flow of energy into the divertor (the D_α intensity is proportional to the product of the neutral atom and ion densities and is therefore a measure of the recycling activity). This is also reflected by the thermographic measurements: after a drop of the plate surface temperature at the end of the L-phase, sudden temperature increases are observed exactly correlated in time with the appearance of D_α bursts in the divertor. These increases happen within a time span of 400 μs (the scan time). This means that the energy

flux into the divertor during a burst lasts for 400 μs at most and it may even be shorter. In most cases, in the interval between two subsequent scans, the temperature may rise and drop again, i.e. the measurement may record the real temperature maximum only by chance. This may give an explanation for the very different calculated shapes of energy deposition profiles of subsequent bursts. To get an idea if a systematic shape of the deposition profiles might possibly be masked by the insufficient temporal resolution of the measurement, calculated profiles of about 20 bursts in a particular H-phase were averaged to a 'representative' burst profile. Figure 34 shows an example of a profile obtained by this method. In H-phases with high burst frequencies, the profile width tends to be several centimetres (up to 6 or 7), and even a single burst may display several deposition maxima. The number of maxima may be between one and, say, five. For subsequent tokamak discharges the 'reepresentative' burst profile often looks qualitatively similar, but no really systematic behaviour is found.

During a burst, energy fluxes may attain values of several MW/cm^2. For ASDEX discharges with high burst repetition rates (20 bursts or more in the H-phase) as shown in Figs. 33 and 34, the thermographic apparatus does not allow energy fluxes to the plate to be measured between bursts. As discussed later in detail, the surface temperature decrease after deposition of energy by a burst is found to be faster than expected from diffusion of the heat wave into the bulk of the plate alone, so that the numerical calculation yields negative energy fluxes for the period of such enhanced dissipation (a few milliseconds). In the examples of our figures this period usually extends to the time of the next ELM outburst. Nevertheless, Fig. 34 also shows energy flux profiles calculated from n_{ed} and T_{ed} profiles taken by probes between bursts. They show that for burst-free discharge periods energy fluxes comparable to fluxes during the ohmic heating phase are to be expected.

- H-phases with low burst activity

Figures 35a and 35b show the divertor D_α and the energy flux to the plates for a discharge with a long 'quiet' H-phase interrupted by one single burst. Judging the energy deposition calculated for this particular case, one should remember that all statements concerning burst energy fluxes have to be treated very carefully, on the one hand

owing to the insufficient temporal resolution, and on the other owing to the suspicion that the physics of energy deposition on the short time scales involved may not be completely understood. K. Lackner proposed overcoming the disadvantage of too long scanning times by observation of the temperature drop on the plates after the burst energy has been deposited /18/. If you consider the plate to extend from y = 0 to infinity (a good approximation for times smaller than the diffusion time to the back surface, which is a requirement excellently fulfilled for the time-scale of interest for burst phenomena), the surface temperature of the plate is given by /9/

$$T_s(t) = \frac{\sqrt{K}}{K\sqrt{\pi}} \int_o^t Q_s(t_1) \frac{1}{\sqrt{t-t_1}}\, dt_1 + T_{so} \,, \qquad (35)$$

where T_{SO} is the temperature at $t_1 = 0$ (immediately before the burst arrives). Let the energy deposition by the burst last from $t_1 = 0$ to $t_1 = t_2$ (no deposition afterwards), then the integration must only be carried out to the upper limit t_2. For times t large compared with all possible t_1, i.e. times when the heat pulse has already been switched off for some time, the surface temperature is

$$T_s(t) - T_{SO} \approx \frac{\sqrt{K}}{K\sqrt{\pi}} \frac{1}{\sqrt{t}} \int_o^{t_2} Q_s(t_1)\, dt_1 = \frac{\sqrt{K}}{k\sqrt{\pi}} \frac{1}{\sqrt{t}} E_s, \qquad (36)$$

where E_S is the energy density deposited on the plate by the burst. Thus, it should be possible to obtain E_S, in spite of the insufficient temporal resolution of the measurement, by plotting $T_S(t) - T_{SO}$ versus t.

However, experimentally observed temperature drops do not exhibit the expected behaviour. They are often much steeper than predicted by eq. (36) (see Fig. 36). Since one of the conditions for the validity of eq. (36), $t \gg t_1$, is obviously not very well fulfilled for the temperatures taken at t = 0.4 and 0.8 ms, we checked the influence of this violation by considering the extreme model case of an energy flux constant between t = 0 and 0.4 ms and zero otherwise. Equation (35) can be solved analytically for this case and yields the temperature drop shown in the theoretical curve of Fig. 36 . The temperature adjusts to a $t^{-1/2}$ dependence very rapidly (approximately after 0.4 ms) though the decrease is much faster for the first 0.4 ms after switch-off of the model pulse. In the experiment the transition to the $t^{-1/2}$ behaviour was generally

not observed; in most analyzed situations, the temperature drop remained almost as steep as at the beginning until T_{S0} was reached again. Figure 37 shows a profile of the temporal dependence of the temperature drop.

The question arises what physical mechanism could be responsible for the observed result. We have considered two possibilities: coating of the titanium plate by some thin surface layer with different thermal properties, and influence of surface roughness. A surface layer (for instance, titanium oxide, or a layer containing implanted hydrogen atoms) would probably influence the temperature drop only for time spans shorter than those of interest here. After the heat wave has diffused through the layer, the surface temperature would be dominated by the coupling of the layer to the bulk of the plate material, and the temporal dependence of T_S would be $t^{-1/2}$. However, the temperature drop is irregularly fast for at least 2 ms, which corresponds to a diffusion length $\Delta y = \sqrt{\Delta t \cdot 2\kappa} \approx 200$ µm (provided the thermal constants of the hypothetical layer are not too different from those of pure titanium). This is far too large for the thickness of any imaginable layer.

A second possibility is microscopically inhomogeneous power flow to the surface due to surface roughness. The magnetic flux lines intersect the plates at a grazing angle of about 3°. This means that only part of a rough surface would be directly hit by the power flow, while the remainder would be hidden in a 'shadow'. Two surface elements, one heated to a uniform temperature by a direct, homogeneous heat flow, the other heated to some temperature distribution by the same amount of energy inhomogeneously deposited, emit different infrared radiation densities in the wavelength interval for which the detector of the thermographic system is sensitive. Thus, different energy flux densities are derived for both surface elements. We now try to estimate the effect quantitatively.

Assume that a rough surface element representing one profile point has a homogeneous temperature T_1 before the power flux is switched on. Then, the deposition of some energy flux on only half of the surface (owing to its grained structure) causes the temperature to rise to a new value T_2 at the illuminated spots, whereas it remains unchanged elsewhere. The radiation energy per unit solid angle in the wavelength interval $\lambda \ldots \lambda + d\lambda$ emitted by this piece of surface is thus

$$K_\lambda \cdot d\lambda \sim \left(\frac{1}{e^{\frac{hc}{\lambda k T_1}} - 1} + \frac{1}{e^{\frac{hc}{\lambda k T_2}} - 1}\right) \cdot d\lambda \,, \tag{37}$$

which - for the temperatures of interest here - is well approximated by

$$K_\lambda \cdot d\lambda \sim \left(e^{-\frac{hc}{\lambda k T_1}} + e^{-\frac{hc}{\lambda k \cdot T_2}}\right) \cdot d\lambda \,. \tag{38}$$

If the surface element is smooth, it will be illuminated homogeneously, and both parts will assume the same temperature T_H. The surface will then radiate according to

$$K_{H\lambda} \cdot d\lambda \sim 2 \cdot e^{-\frac{hc}{\lambda k \cdot T_H}} \cdot d\lambda \,. \tag{39}$$

We are interested in the difference between expressions (38) and (39) for the same amount of energy incident on the surface. Let the temperature before the onset of energy flux be T_1 = 350 K. In the case of inhomogeneous illumination, let the quantity of energy be such that one half of the surface element is heated to 500 K. If the surface element were smooth, the same amount of energy would heat the entire element to (500 - 350)/2 = 425 K (diffusion of heat into the bulk neglected). Evaluation of expressions (38) and (39) shows that the ratio of the radiation intensities for inhomogeneous and homogeneous energy flux absorption is $K_\lambda / K_{H\lambda} \approx 1.5$. Inhomogeneous absorption therefore causes overestimation of the energy flux. In our example, the wrong assumption of a uniform temperature rise on the entire surface element (though only part of the observed element may have risen in temperature) leads to the result that the temperature is 452 K homogeneously, and the energy flux is overestimated by a factor of (452 - 350)/(425 - 350) = 1.3.

The preceding discussion shows that inhomogeneous power deposition due to a structured surface may indeed lead to overestimations of the average temperature, and hence the incident energy, until the temperature within a single measuring point has become uniform. On the other hand, the effect is by no means dramatic so that it remains questionable if this is the only mechanism responsible for the observation of too fast temperature drops after energy depositon during ELM's and the drastic deviations from the expected $t^{-1/2}$ temperature drop. But we should keep in mind that this effect alone might cause

errors in the energy flux calculations of at least 30 %. Again, the time interval for which the accelerated temperature drop is observed (2 ms) allows one to estimate the diffusion length parallel to the surface and, thus, the grain size characterizing the roughness. The resultant 200 µm is too large to be realistic and provides another indication that the true deposition mechanism during bursts has not yet been found.

Though this situation - complicated by the unsatisfactory temporal resolution of the power deposition - does not allow one to give an estimation of the power flux during bursts of better than, say, 50 %, the measurements taken during 'quiet' H-phases do indeed allow one to make some interesting statements. Between bursts, the power flux is approximately reduced to its ohmic value. The probe measurements also show that densities and electron temperatures go down to ohmic values during the quiescent H-phase (see Fig. 27), and that they approximately coincide with the densities and electron temperatures measured between bursts in H-phases with high burst activity (compare Figs. 9 and 27).

The observed power fluxes compare quite well with the plasma temperature and density profiles taken between bursts in the discharges with high ELM activity (see, for instance, the calculated power fluxes in Figs. 30 and 31). A second remarkable result is that the energy content of bursts preceding 'quiet' H-phases and singular bursts interrupting such 'quiet' phases tends to be small owing to the small widths of the power fluxes. Additionally, during the course of 'quiet' phases the maximum of the deposition moves considerably below the calculated intersection of the separatrix with the plates (Figs. 35a, 35b). Perhaps this observation has to be seen in connection with the possible existence of high electric fields in the divertor, leading to additional drift terms acting upon the scrape-off plasma.

5. Summary

For different situations (ohmic heating, neutral injection, lower hybrid current drive), density and temperature profiles in the divertor were measured. All profiles display a comparable structure, i.e. a peak near the separatrix and a shoulder outside. Depending on the situation, the temperatues in the peak vary between 5 and 30 eV, the densities between

2×10^{12} and 2×10^{13} cm^{-3}. In the OH-phase of the plasma, fast electron fluxes could be detected near the separatrix by means of the probe characteristics. It was shown that the fast electron fluxes from the midplane cannot lead to electrical charging of the divertor plasma either in the OH or in the L or H-phase. On the contrary, the midplane plasma potential near the separatrix shifts about 250 eV to 1000 eV with respect to the vessel potential or the divertor plasma potential.

A comparison between probe and laser scattering measurements shows good agreement. Both methods detect non-Maxwellian electron distribution functions during neutral injection. There is also good agreement between probe and energy flux measurements in the OH-phase. During the L-phase of neutral injection, the measured energy deposition is larger than calculated from the probe data. The difference is traced back to fast electrons from the midplane. The energy deposition in the H-phase between bursts is comparable to that in the OH-phase. During a burst, the energy deposition is about 50 times larger than in the quiescent periods of the H-phase.

References

/1/ Steuer und Röhr, to be published.

/2/ E.O. Johnson and L. Malter, Phys. Rev. 80, 58 (1950)

/3/ U. Ditte, Thesis, Universität Essen (1983).

/4/ J.G. Laframboise, UTIAS Report No. 100, Inst. for Aerospace Studies, University of Toronto (1966).

/5/ C.H. Reinsch, Numerische Mathematik 10, 177 (1967).

/6/ H. Murmann, M. Huang, IPP-Bericht IPP III/95 (1983).

/7/ E.R. Harrison and W.B. Thompson, Proc. Phys. Soc. London 74, 145 (1959)

/8/ J.G. Andrews, J.E. Allen, Proc. Roy. Soc. Cond. A. 320, 459 (1971)

/9/ E.R. Müller, K. Steinmetz, B.K. Bein, IPP Report III/97 (1984).

/10/ B.K. Bein, E.R. Müller, J. Nucl. Mat. 111 & 112 (1982) 548.

/11/ K. Lackner, private communication

/12/ W. Eckstein, H. Verbeek, Nucl. Fusion, special issue 1984, p. 12.

/13/ D. Heifetz, K. Lackner, K.G. Rauh, W. Schneider, Proc. 11th European Conference on Controlled Fusion and Plasma Physics, Aachen 1983, p. 389.

/14/ W. Schneider, D. Heifetz, K. Lackner, J. Neuhauser, D.Post, K.G. Rauh, J. Nucl. Mat. 121, 178 (1984).

/15/ C.E. Singer, K. Mann, to be published.

/16/ W. Eckstein, priv. communication.

/17/ K. McCormick, H. Murmann, M. ElShaer, ASDEX and NI Team, Princeton 1983, J. Nucl. Mat. 121 (1984) 48.

/18/ K. Lackner, priv. communication.

Acknowledgement

The authors express their thanks to the entire ASDEX team. They acknowledge the encouragement and support given by G. v. Gierke and M. Keilhacker. Thanks are also due to H. Volkenandt for preparing the drawings and to I. Hermann for handling the secretarial work. They acknowledge the engineering work of R. Komen.

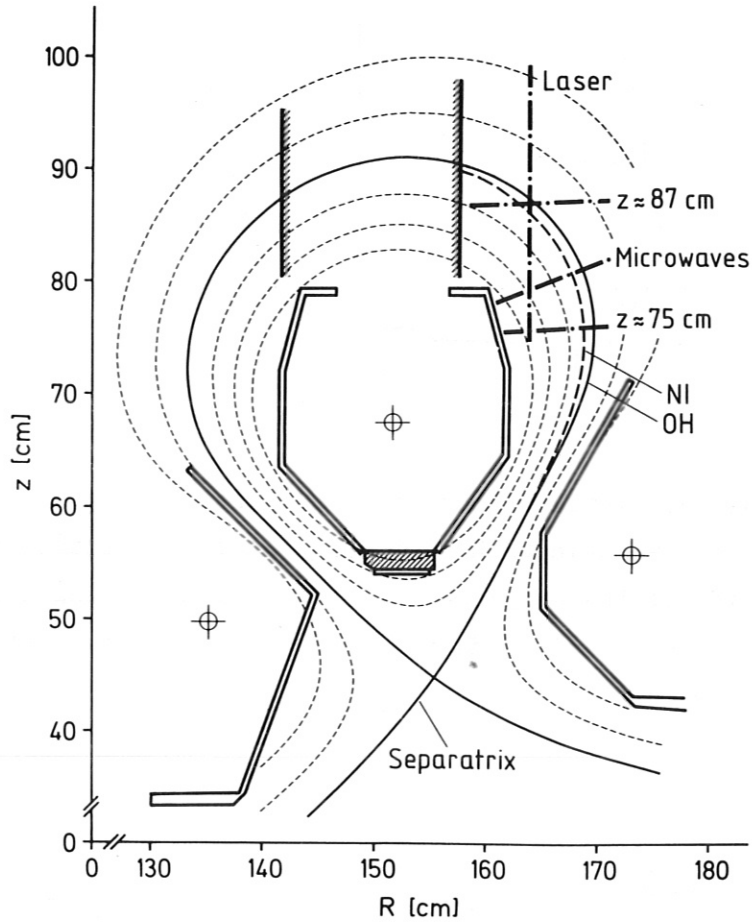

Fig. 1: Schematic of the divertor region showing the location of the different n_{ed} and T_{ed} measurements.

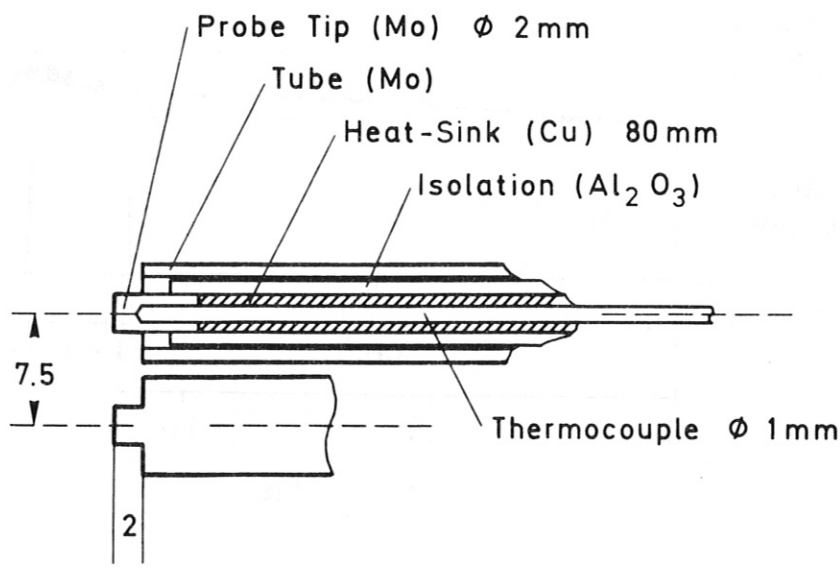

Fig. 2: The Langmuir probe design.

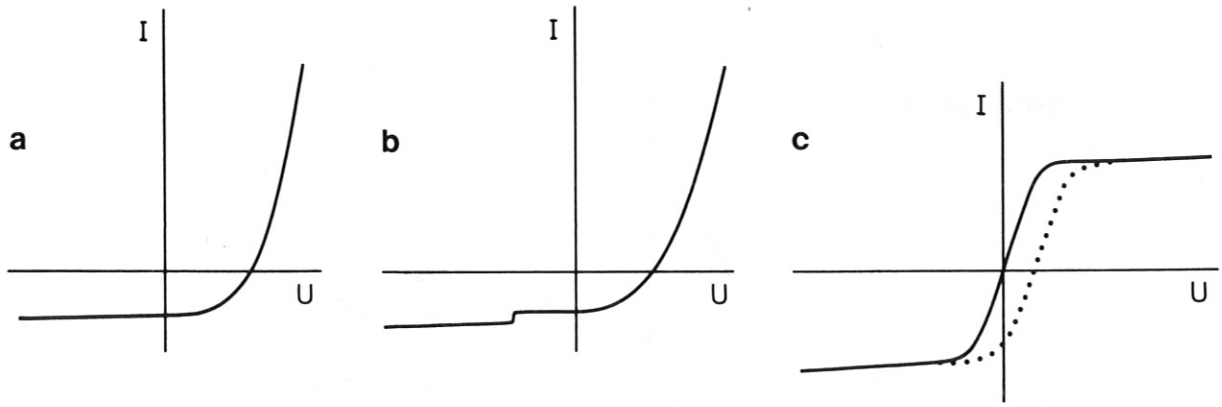

Fig.3a: Characteristic without fast electron component.

3b: Characteristic with monoenergetic fast electron component.

3c: Shift of the origin of a characteristic. Such shifts can occur when potential gradients or locally varying distribution functions are present.

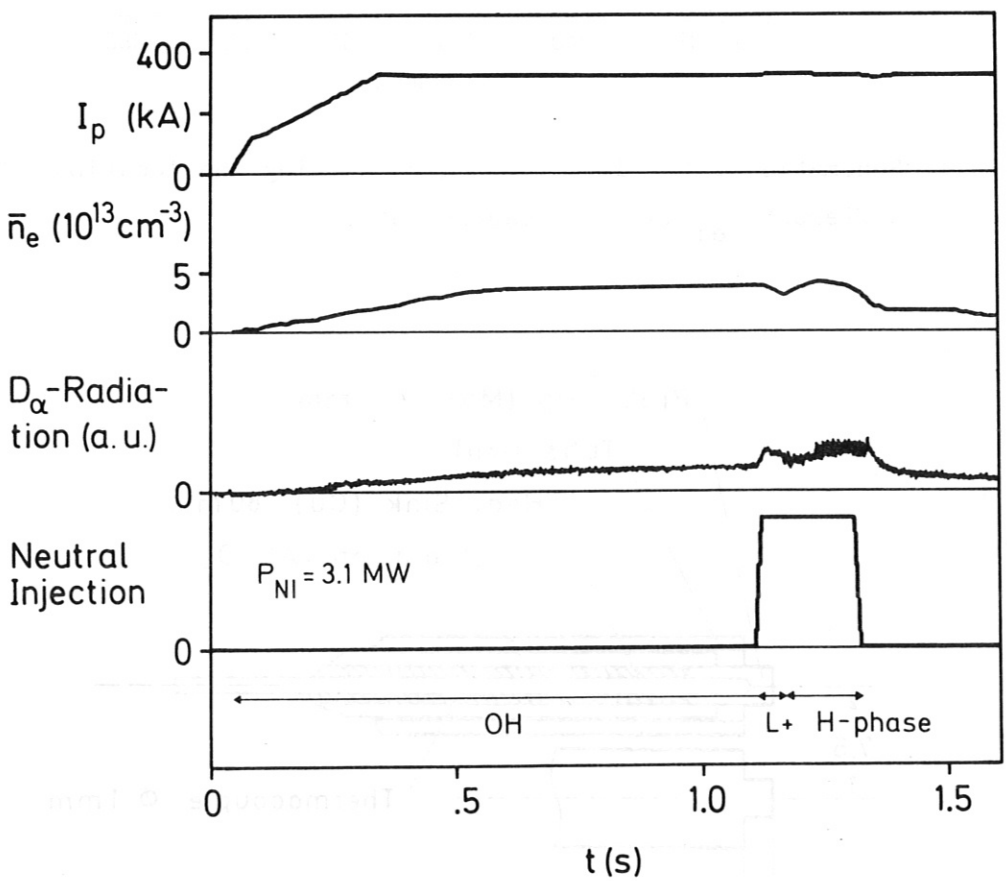

Fig. 4: Typical temporal development of plasma current, density, and D_α radiation during the 'neutral injection series' #10804 - 10833.

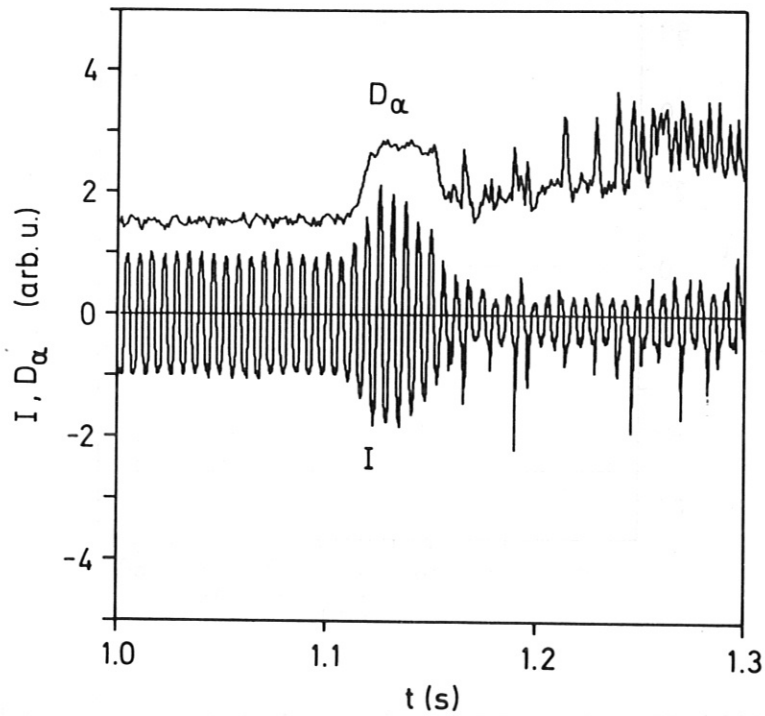

Fig. 5: Typical temporal development of probe current and D_α radiation during the OH, L and H-phases.

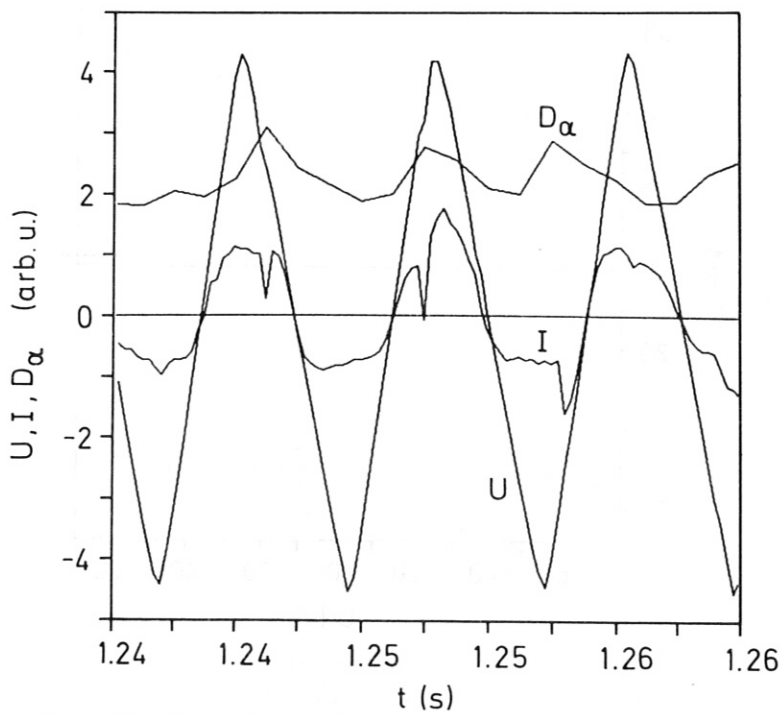

Fig. 6: Typical temporal development of probe voltage, probe current, and D_α radiation during the H-phase. Bursts cause both probe current break-downs and spikes.

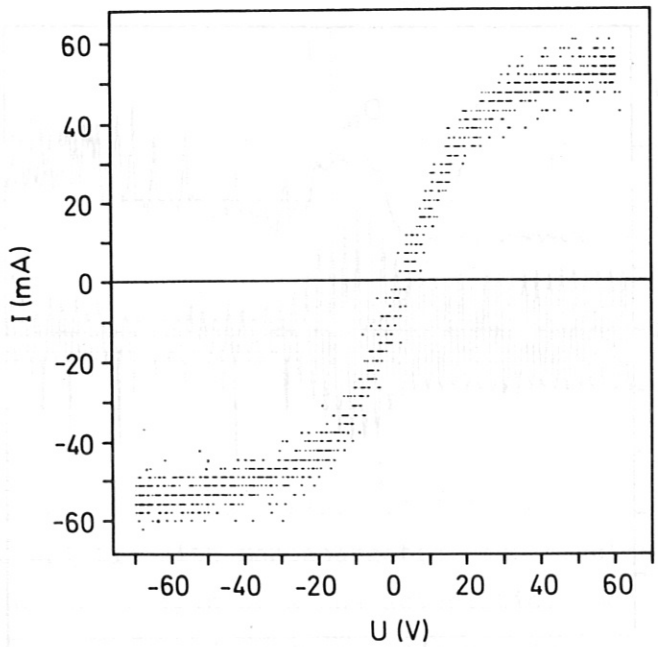

Fig. 7a: Superimposed measuring points from characteristics taken between t = 0.8 and 1.09 s in the OH-phase.

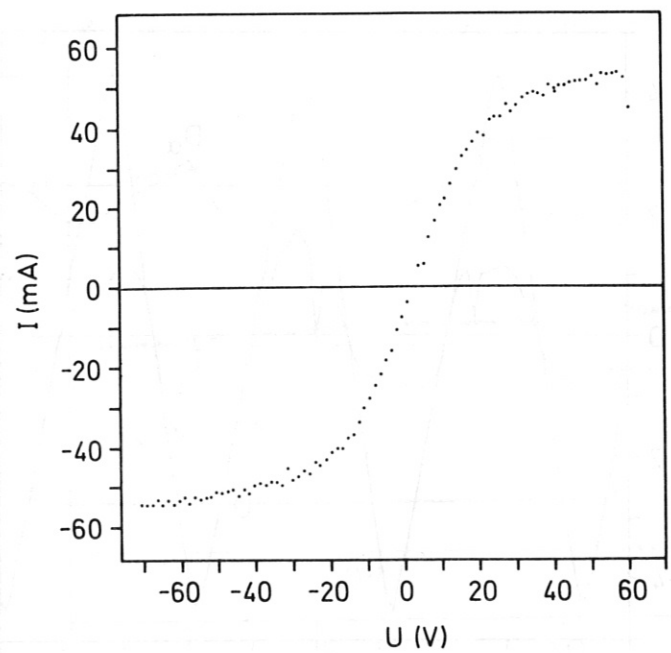

Fig. 7b: Characteristics for the same period as in Fig. 7a. Shown are mean values which were obtained by averaging over current values in succcessive voltage intervals (ΔU = 0.75 V).

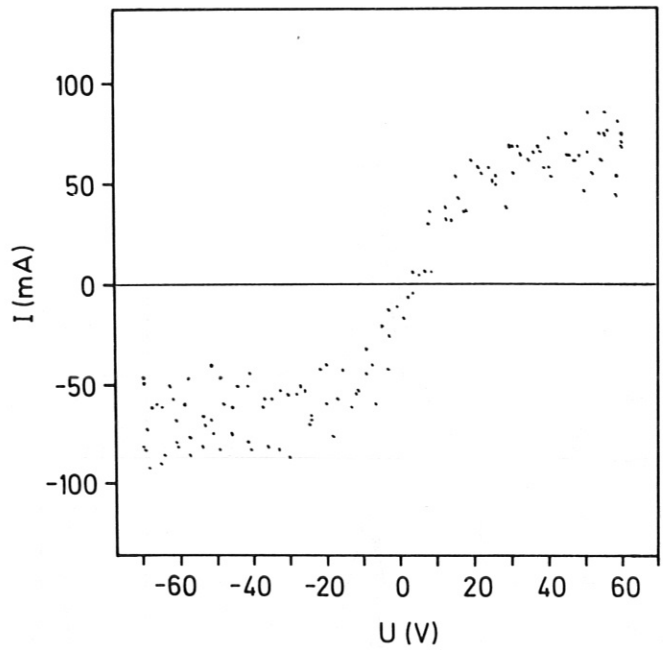

Fig. 8a: Superimposed characteristics during the L-phase (t = 1.125 ... 1.15s).

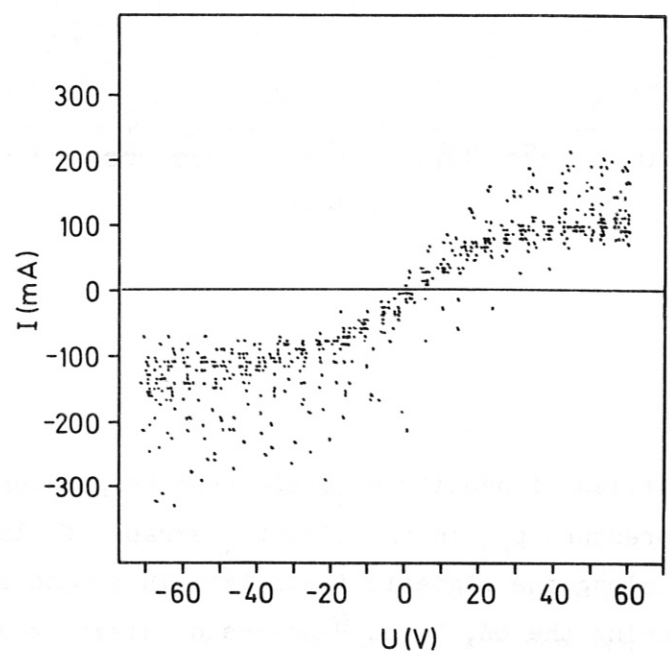

Fig. 8b: Superimposed characteristics during the H phase (t = 1.17...1.3s).

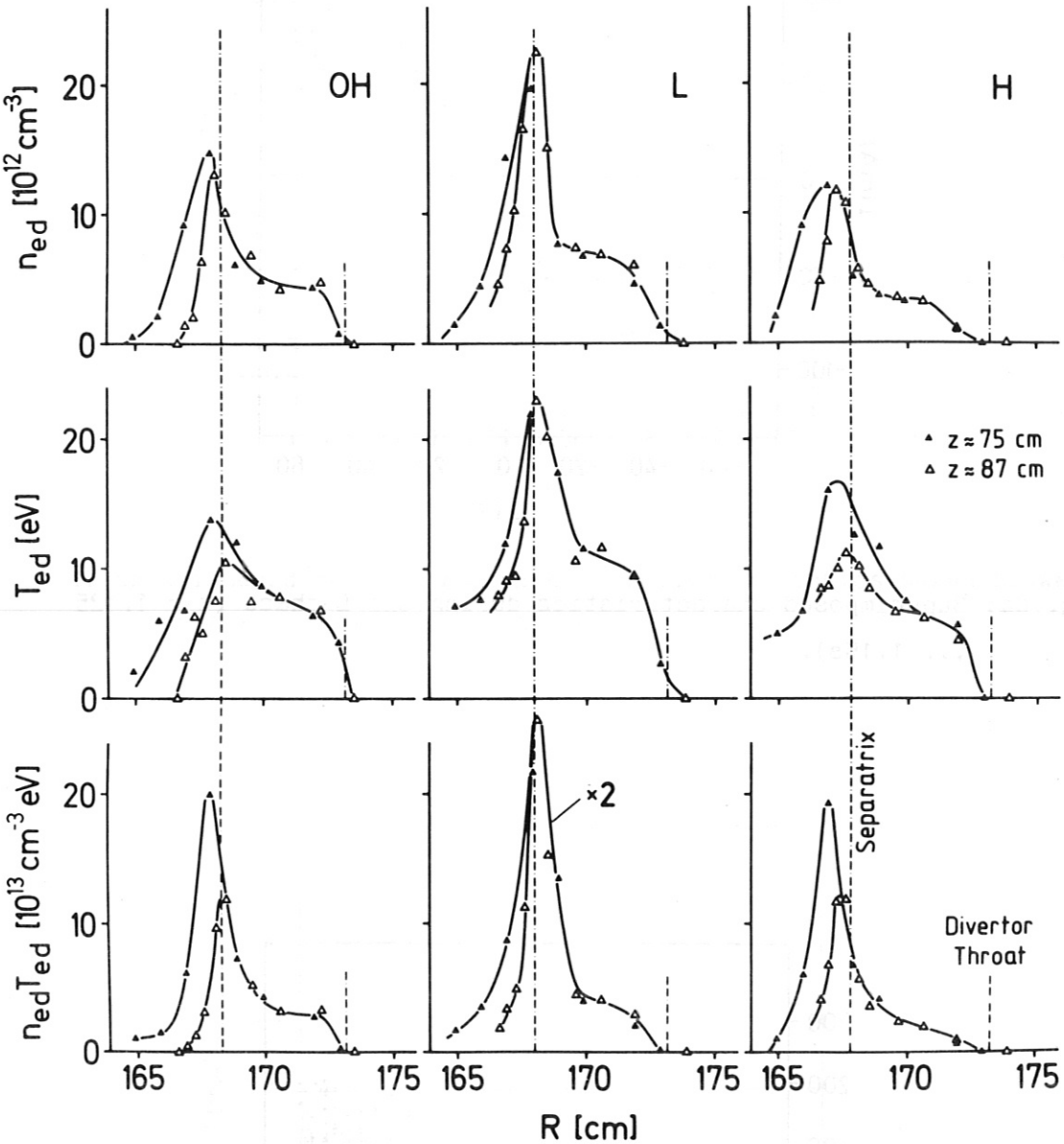

Fig. 9: Radial profiles of density n_{ed}, electron temperature T_{ed} and electron pressure p_{ed} in the divertor scrape-off layer at two positions along the magnetic field ($z \approx 75$ cm and $z \approx 87$ cm, cf. Fig. 1) during the OH, L and H-phases of discharges with I_p = 320 kA, $\bar{n}_e = 3.6 \times 10^{13}$ cm^{-3} and P_{NI} = 3.1 MW. #10804-10833.

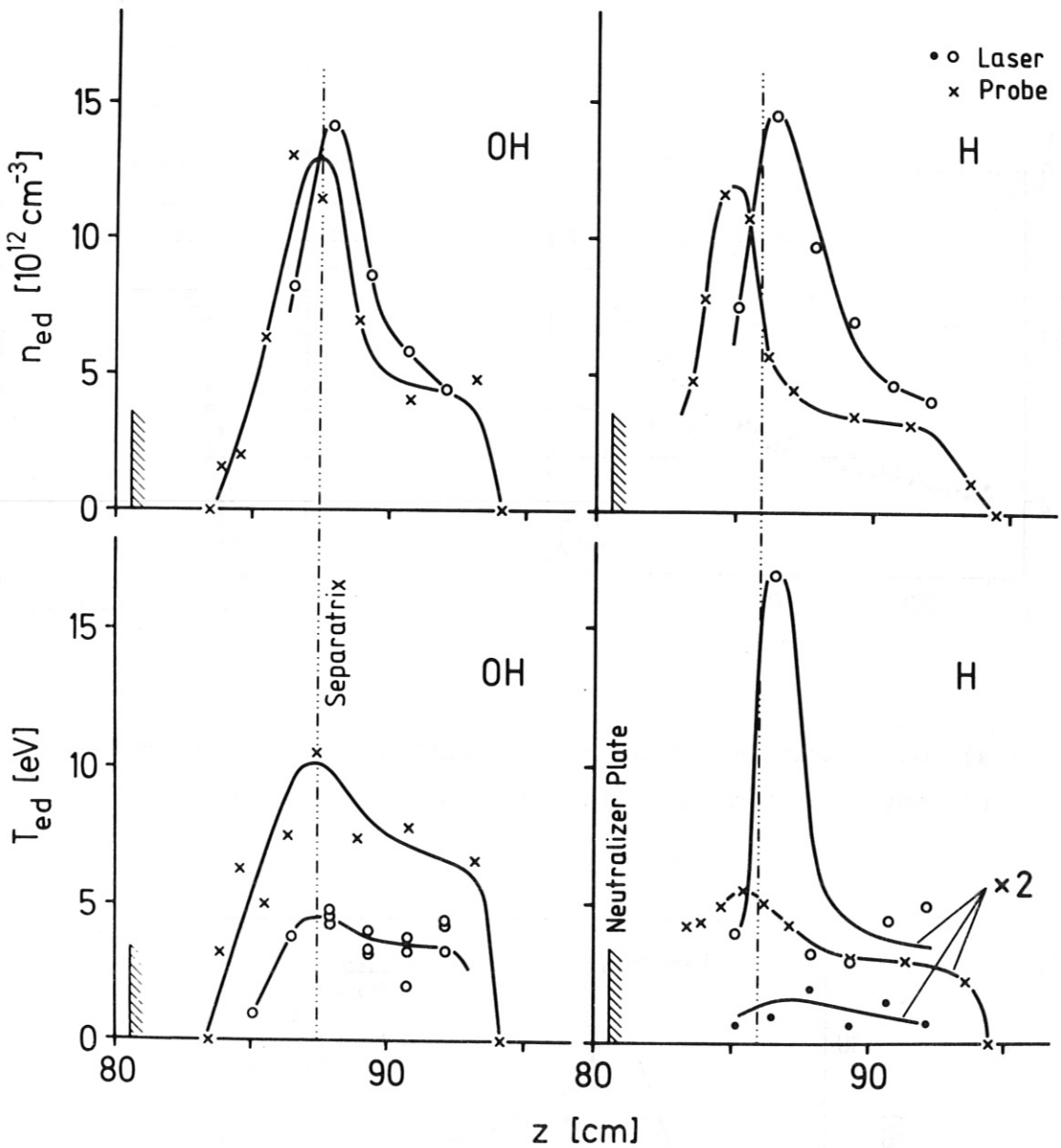

Fig. 10: Comparison of Langmuir and Thomson scattering measurements of density n_{ed} and electron temperature T_{ed} near the neutralizer plate during the OH and H-phases. #10804 - 10833.

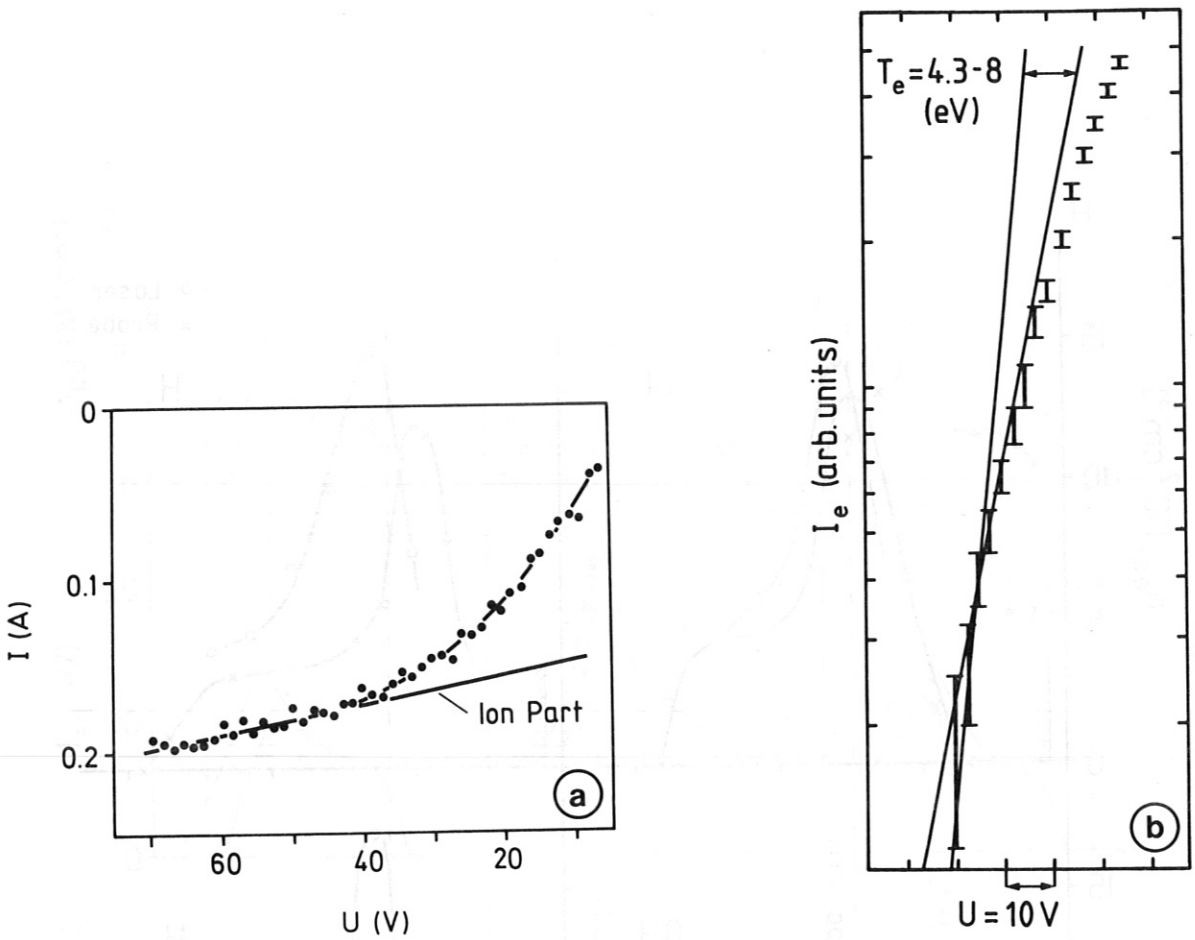

Fig. 11: a) Ion saturation and incipient electron part of a characteristic.
b) Semi-logarithmic plot of incipient electron current.

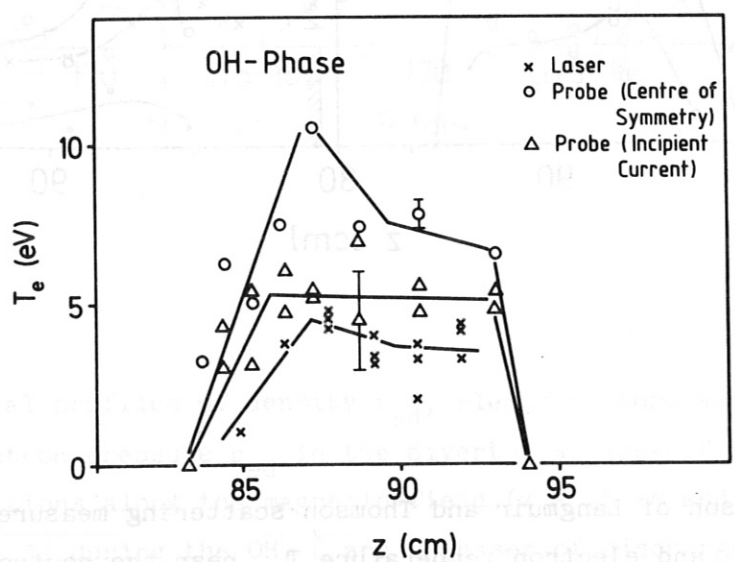

Fig. 12: Electron temperatures measured with probes compared with laser scattering measurements.

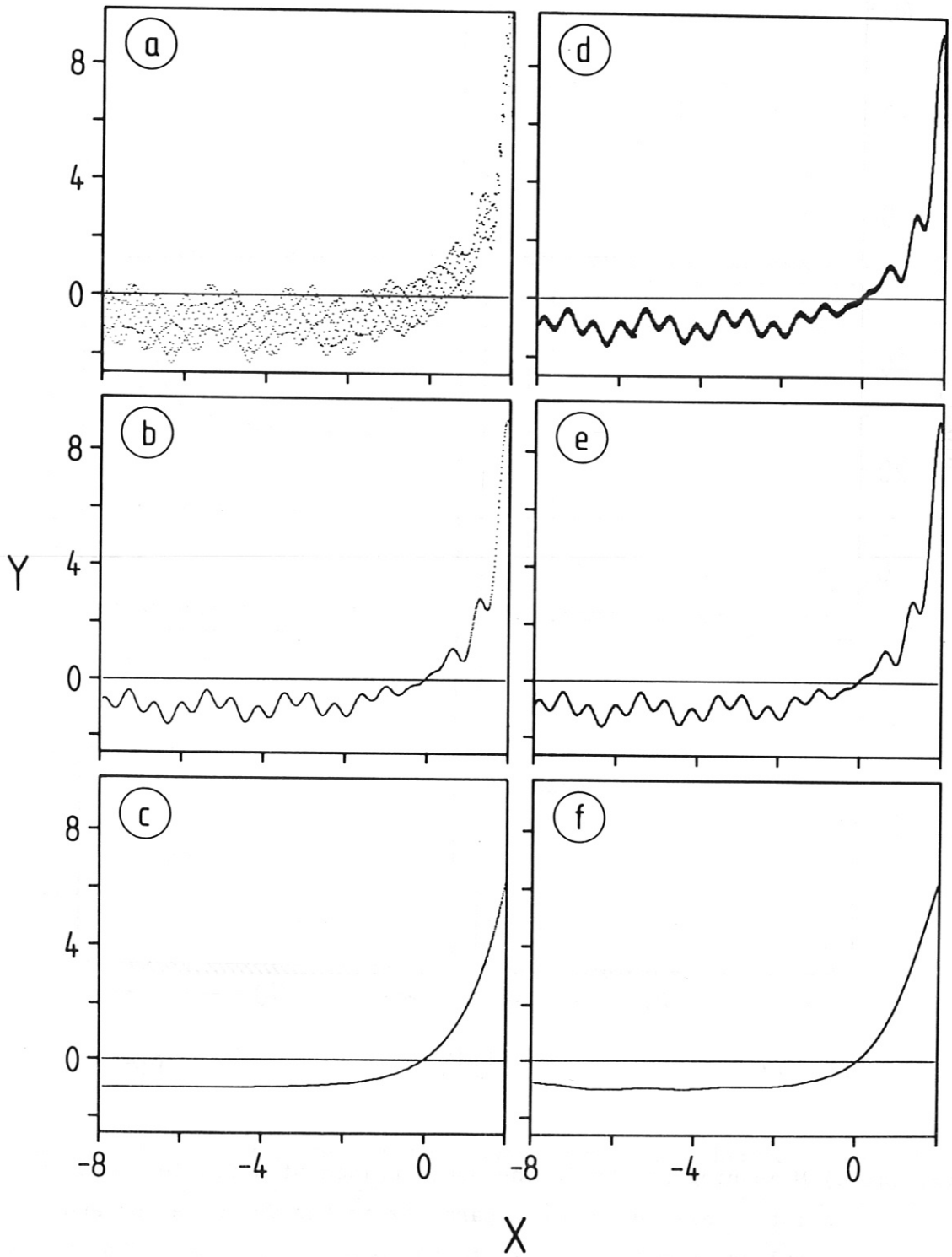

Fig. 13: Test of a spline fit: a) test point distribution to be fitted, b) and c) structures contained in a), d) to f) spline fits to the test point distribution with increasing smoothing parameter.

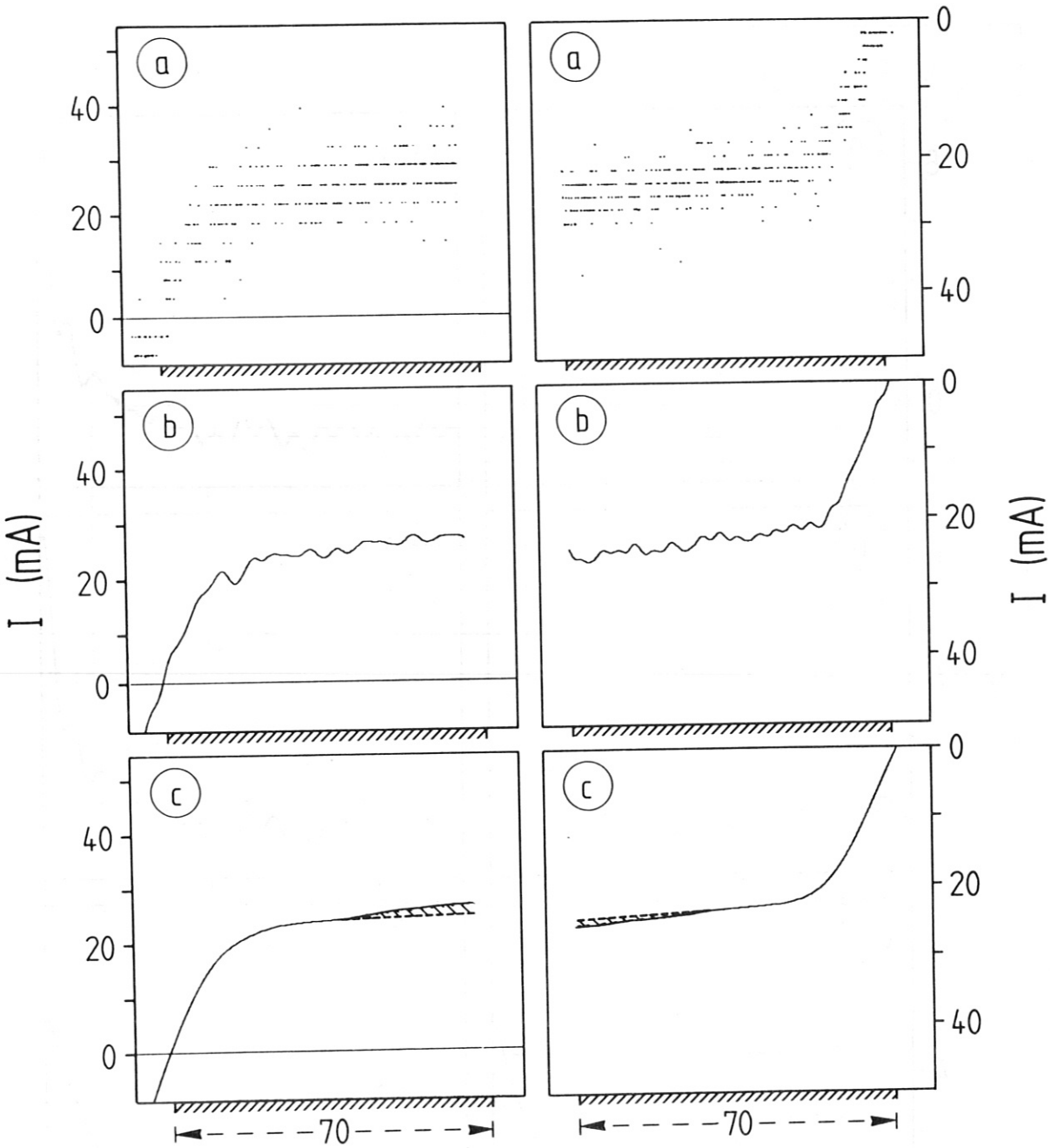

Fig. 14

Fig. 15

Fig. 14: a) Measuring points in the upper branch of a double probe characteristic taken near the separatrix in the OH-phase, b) and c) spline functions fitted to the measuring points. The optimum smoothing c) displays a structure which can be interpreted as a fast electron component (shaded).

Fig. 15: a) Measuring points in the lower branch of the double probe characteristic of Fig. 15, b) and c) spline functions fitted to the measuring points. The optimum smoothing c) displays a structure which can be interpreted as a fast electron component (shaded).

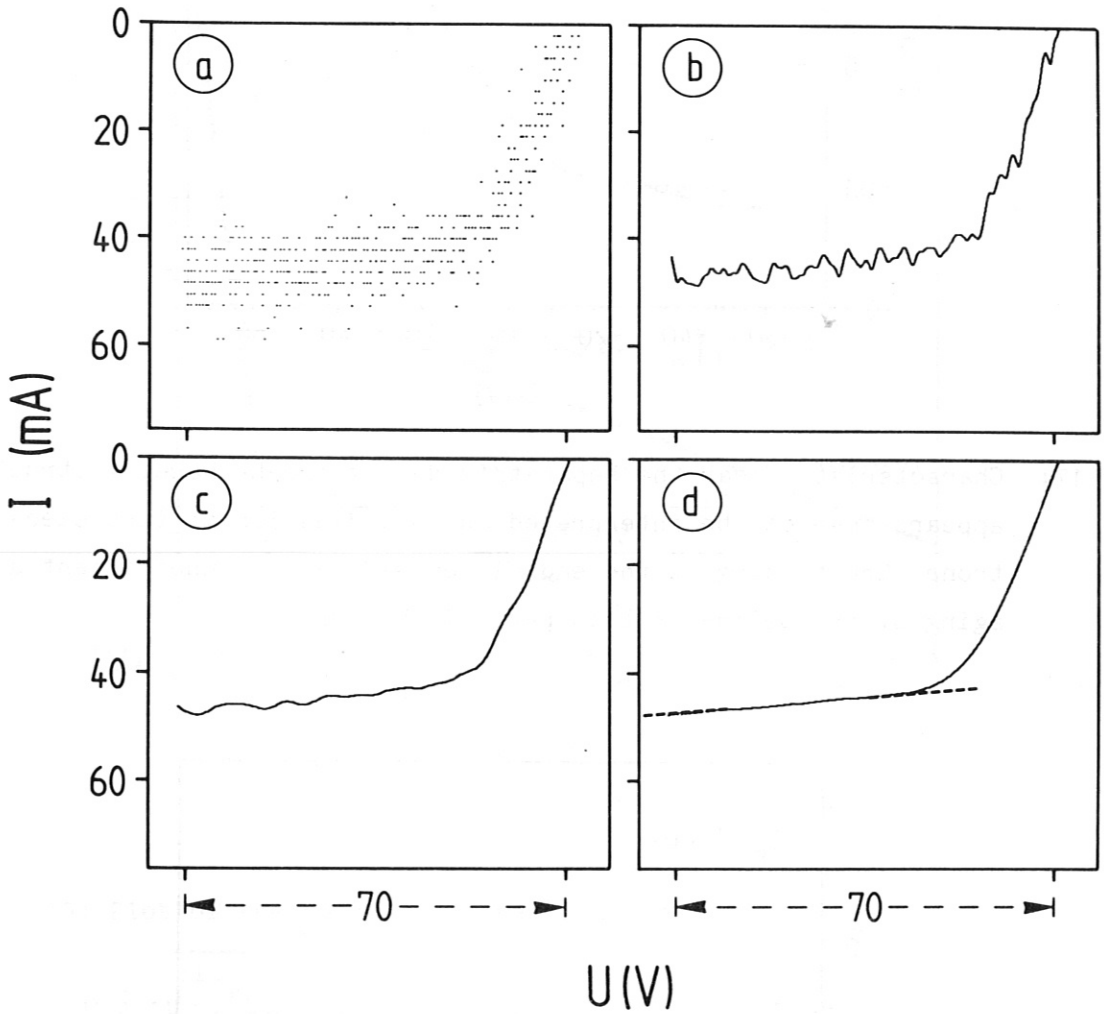

Fig.16: a) Measuring points in the lower branch of a double probe characteristic taken outside the separatrix in the OH-phase, b) - d) spline functions fitted to the measuring points. The optimum smoothing d) does not display a structure in the saturation part.

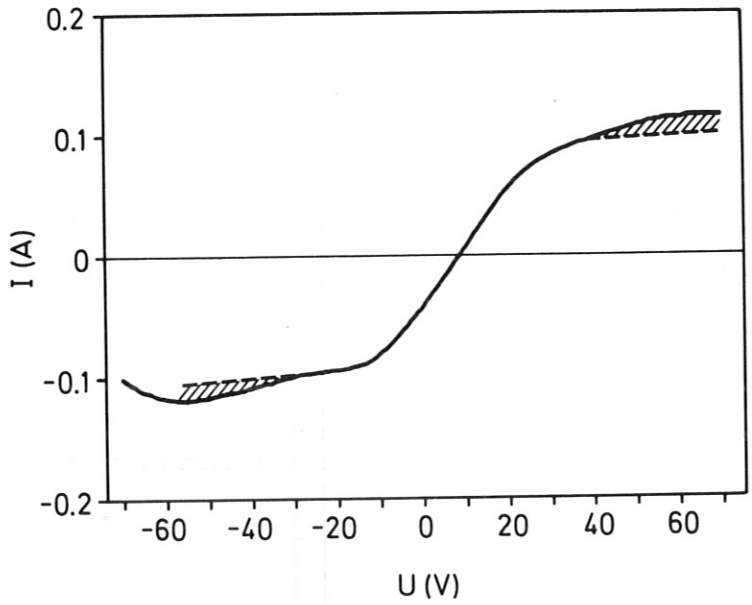

Fig.17: Characteristic near the separatrix during the L-phase. A structure appears that can be interpreted as an indication of fast electrons. The tilting at the ends is caused by the insufficient averaging of the spline in this part of the curve.

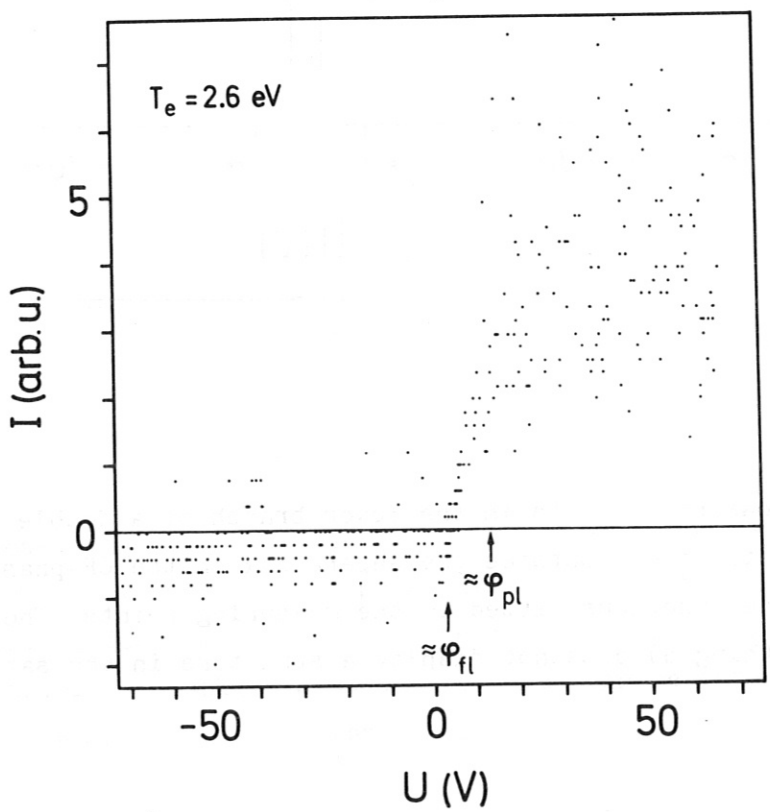

Fig. 18: Measuring points of a single probe characteristic taken in the shoulder of the divertor probe profile.

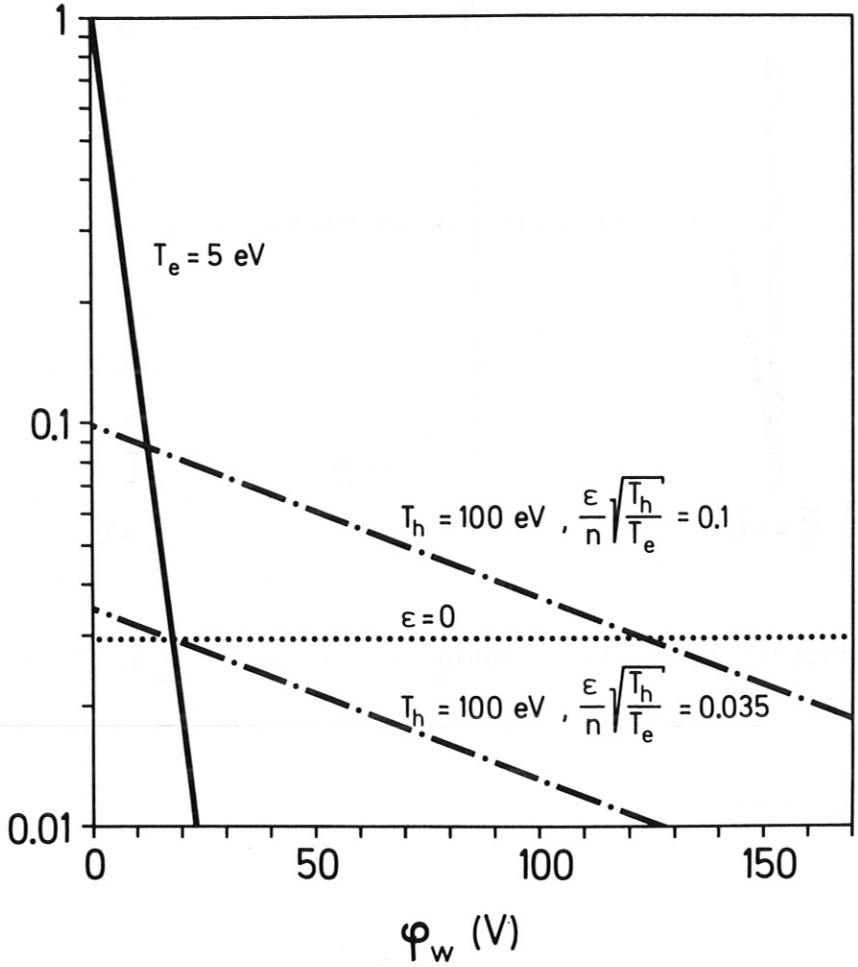

Fig. 19: Plot of the solution of the function

$$\frac{0.5 \cdot \sqrt{\frac{kT_e}{m_i}}}{\sqrt{\frac{kT_e}{2\pi m_e}}}(n + \varepsilon) = e^{-e\varphi_w/kT_e} + \frac{\varepsilon}{n}\sqrt{\frac{T_h}{T_e}}\; e^{-e\varphi_w/kT_h} \qquad \text{with}$$

$$\cdots\cdots = \frac{0.5 \cdot \sqrt{\frac{kT_e}{m_i}}}{\sqrt{\frac{kT_e}{2\pi m_e}}}\,, \qquad -\cdot-\cdot- = \frac{\varepsilon}{n}\sqrt{\frac{T_h}{T_e}}\; e^{-e\varphi_w/kT_h}\,,$$

$---- = e^{-e\varphi_w/kT_e}$. The intersection of the dotted curve with the sum of the dash-dotted and solid curves yields the wall potential φ_w. For $\varepsilon/n\sqrt{T_h/T_e} < 0.035$, the neutralizer plates are not charged by fast electrons any more.

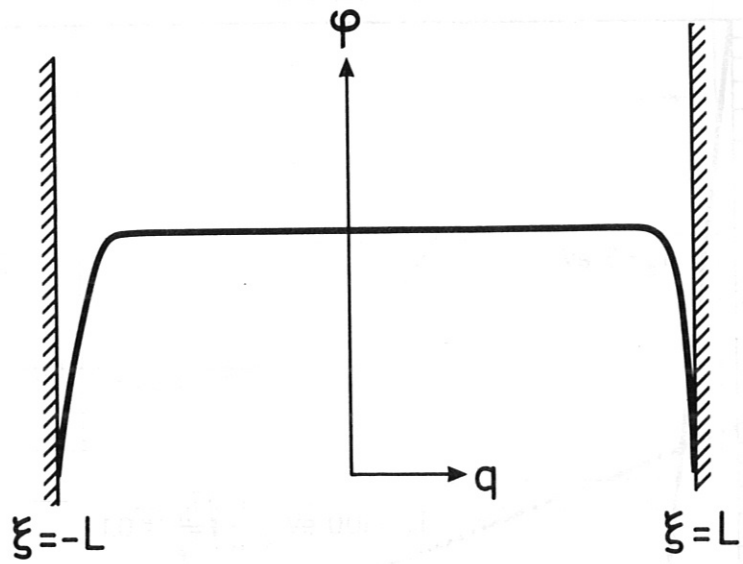

Fig. 20: Illustration of the potential in the Harrison and Thomson model /7/.

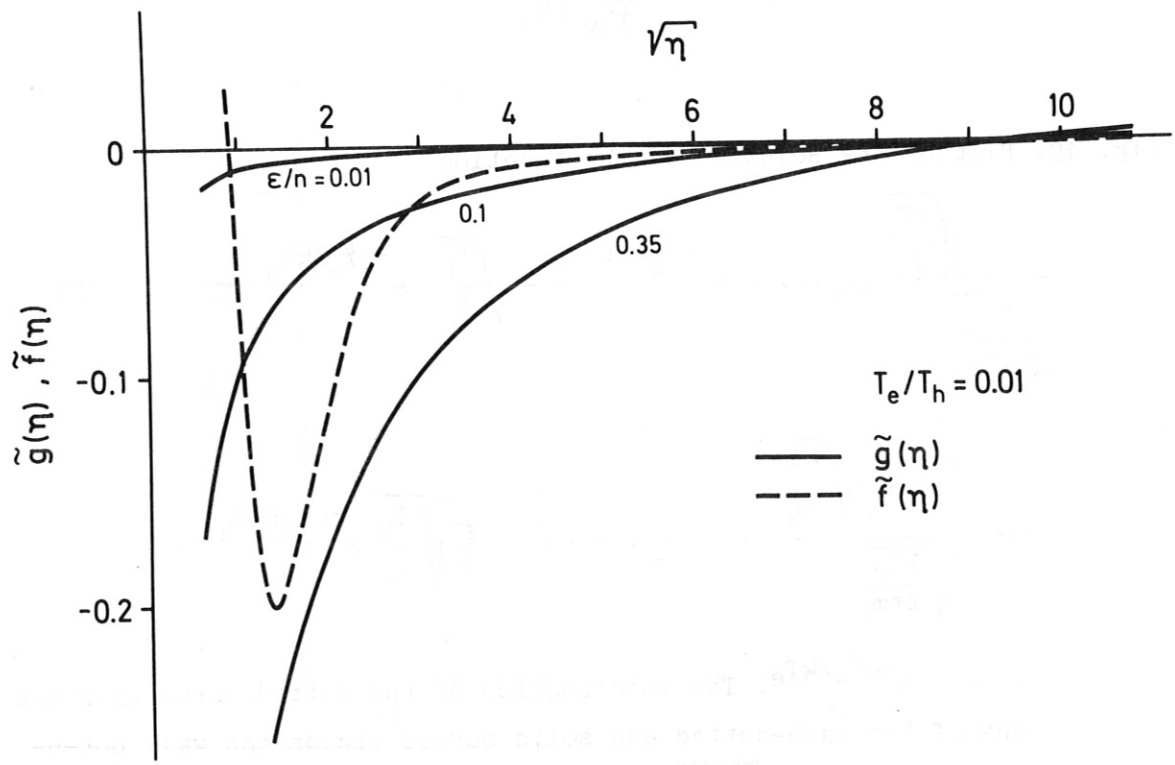

Fig. 21:

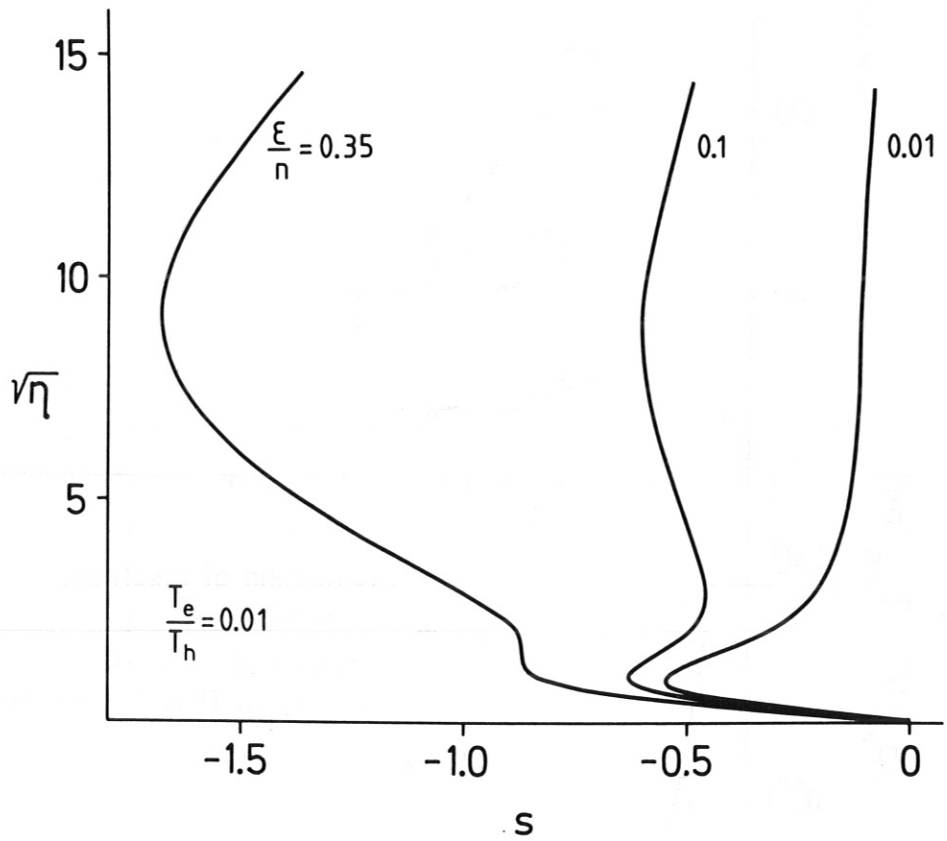

Fig. 22: Potential distribution in the presheath as a function of the normalized coordinate s.

Fig. 21: Potentials at the boundary layer. Solutions of the eq. (16), with

$$\tilde{f}(\eta) = [\eta^{-\frac{1}{2}} - 2\, e^{-\eta}\, D(\sqrt{\eta})] \quad \text{and}$$

$$\tilde{g}(\eta) = -\frac{\varepsilon}{n}\sqrt{\frac{T_e}{T_h}} \cdot [(\frac{T_e}{T_h}\,\eta)^{-\frac{1}{2}} - 2\, e^{-T_e/T_h\,\eta} \cdot D(\sqrt{\frac{T_e}{T_h}\cdot\eta})].$$

The intersections of the dashed with the solid curves give the potentials for which $d\xi/d\eta = 0$.

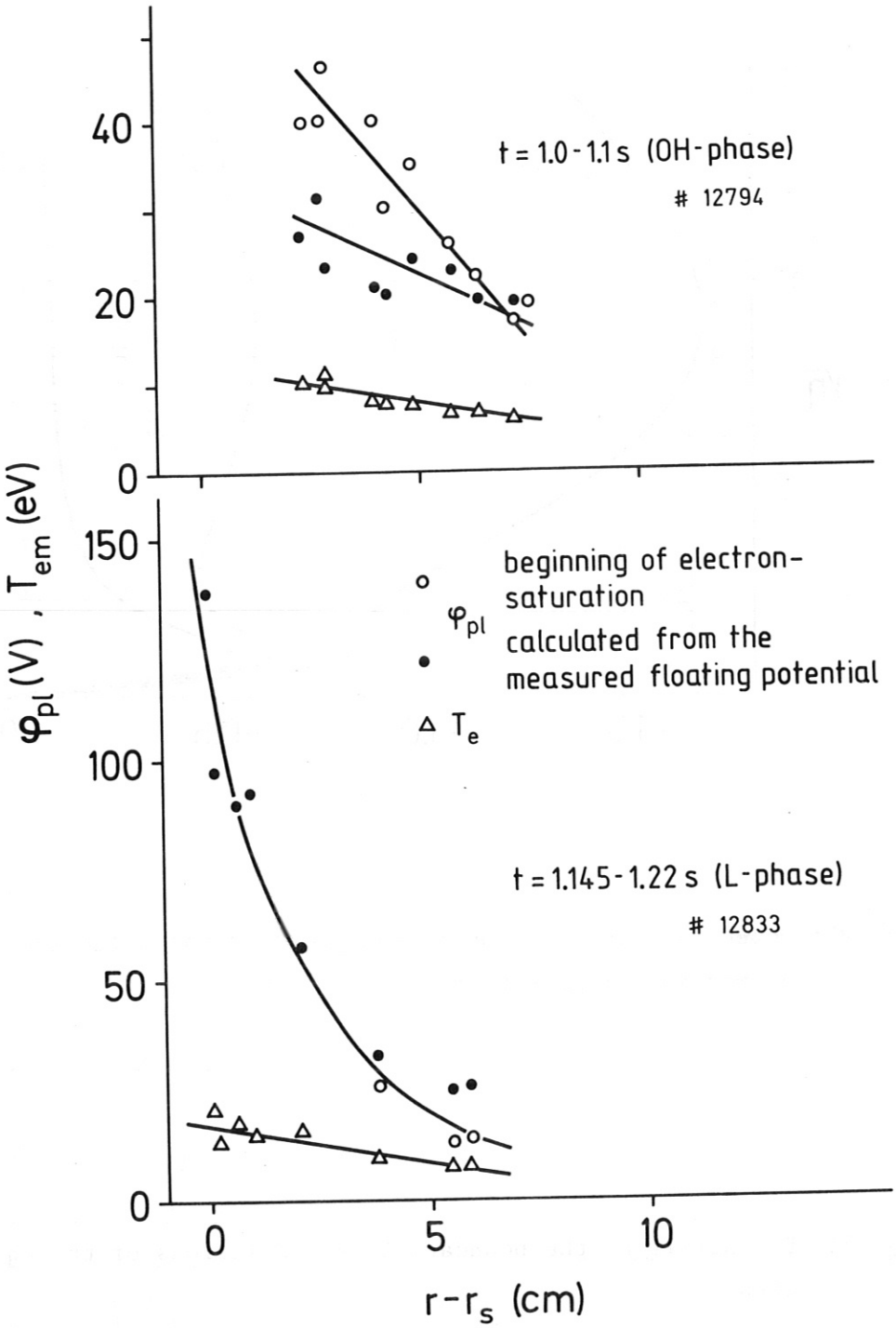

Fig. 23: Measured plasma potentials φ_{pl} and temperatures T_{em} in the midplane during the OH and L-phases of the discharge.

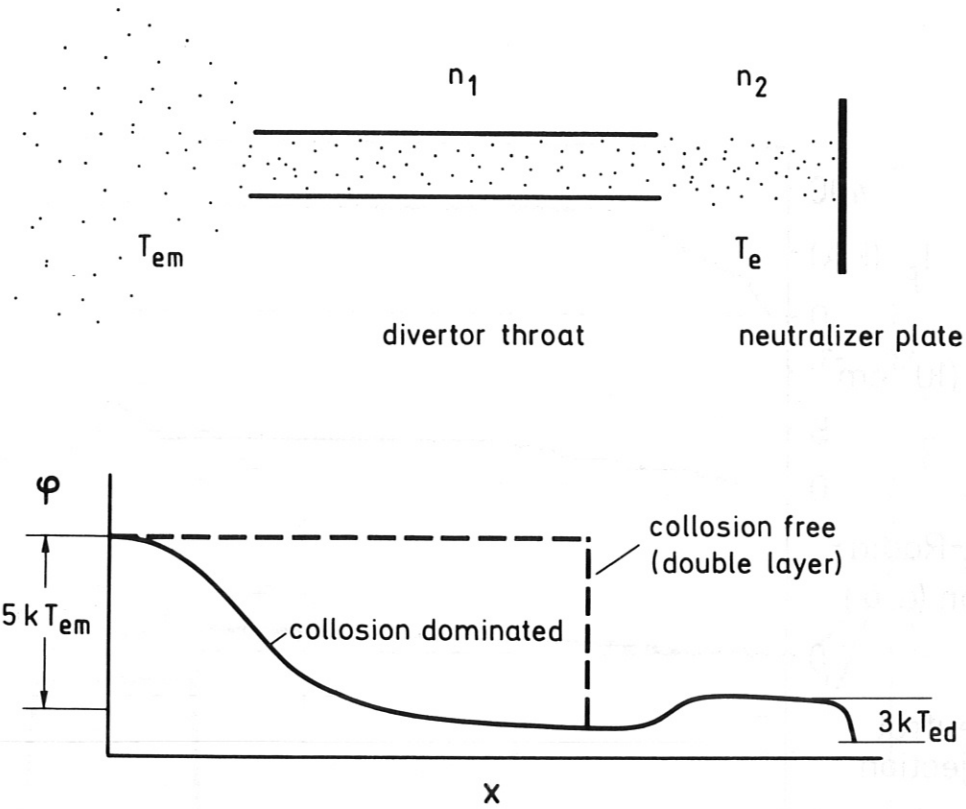

Fig. 24: Potential distribution between the midplane and neutralizer plates.

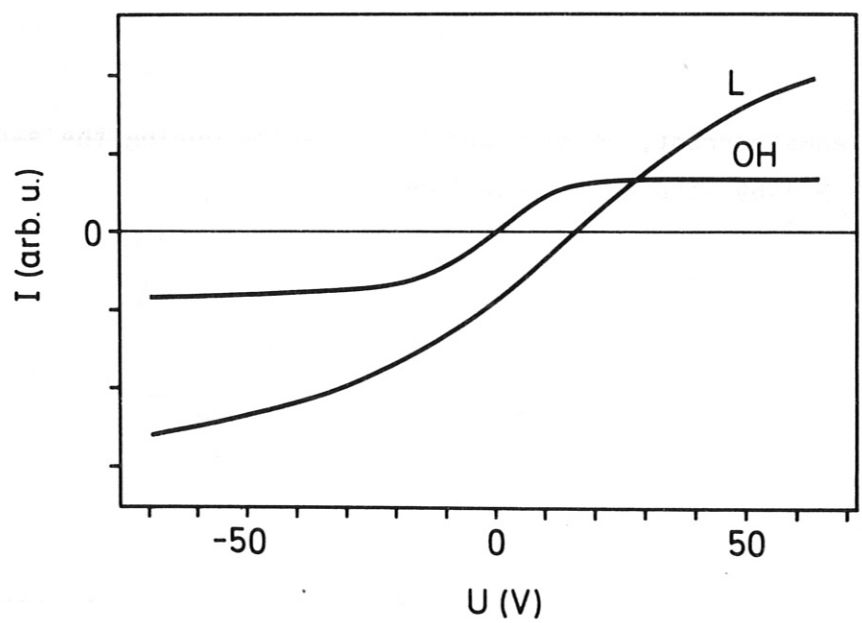

Fig. 25: Shift of the origin of double probe characteristics at the transition from the OH to the L-phase.

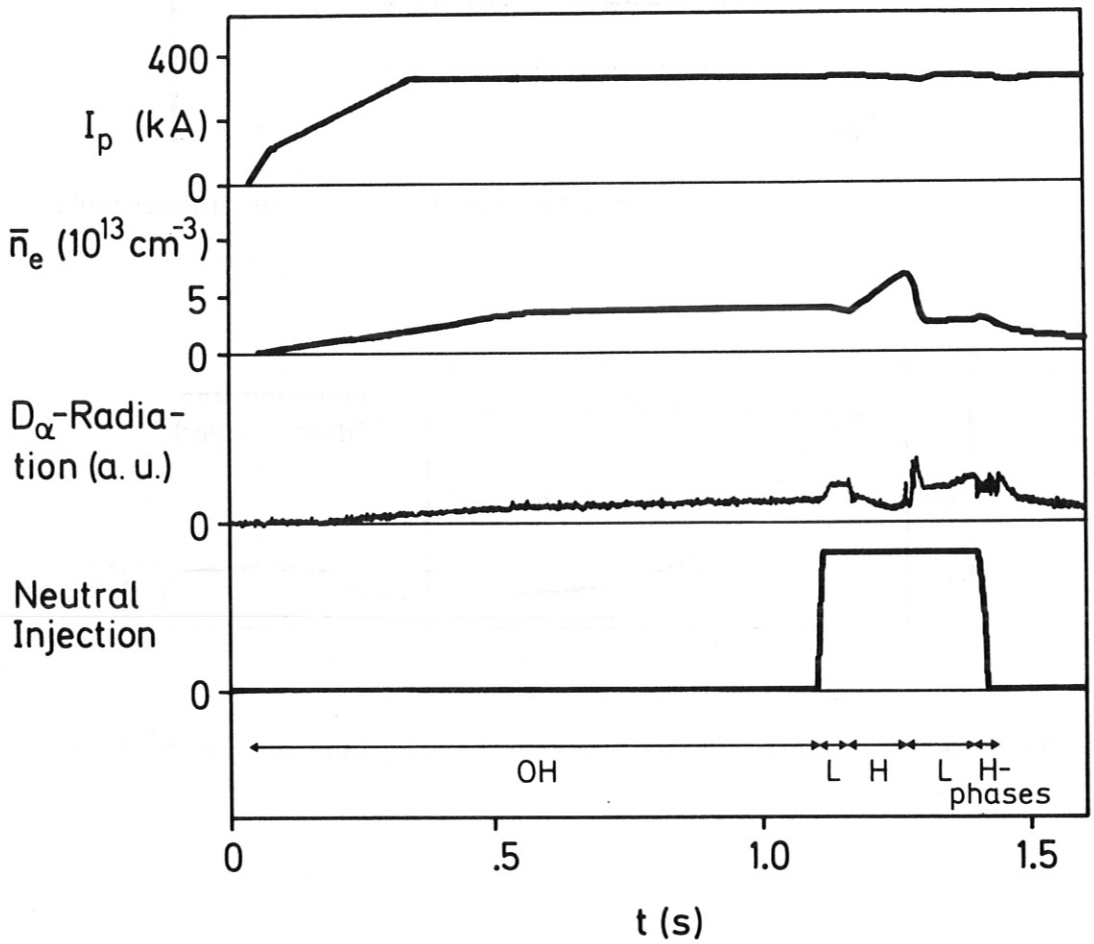

Fig. 26: Plasma current, density and D_α radiation during the series #11437 - #11469 with burst-free H-phases.

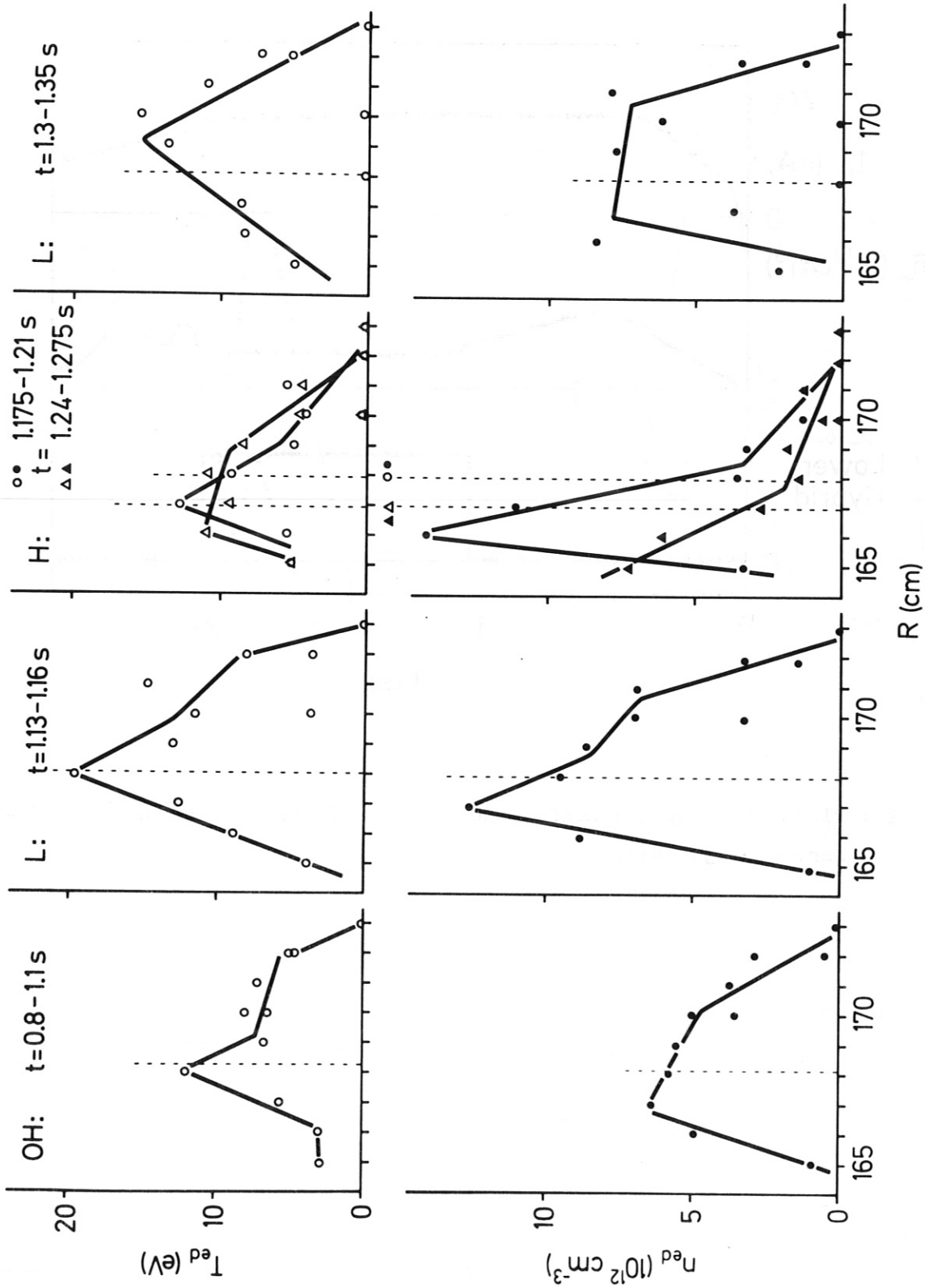

Fig. 27:
Profiles in the divertor at the transitions from the OH to the L-phase and from the L to the burst-free H-phase.

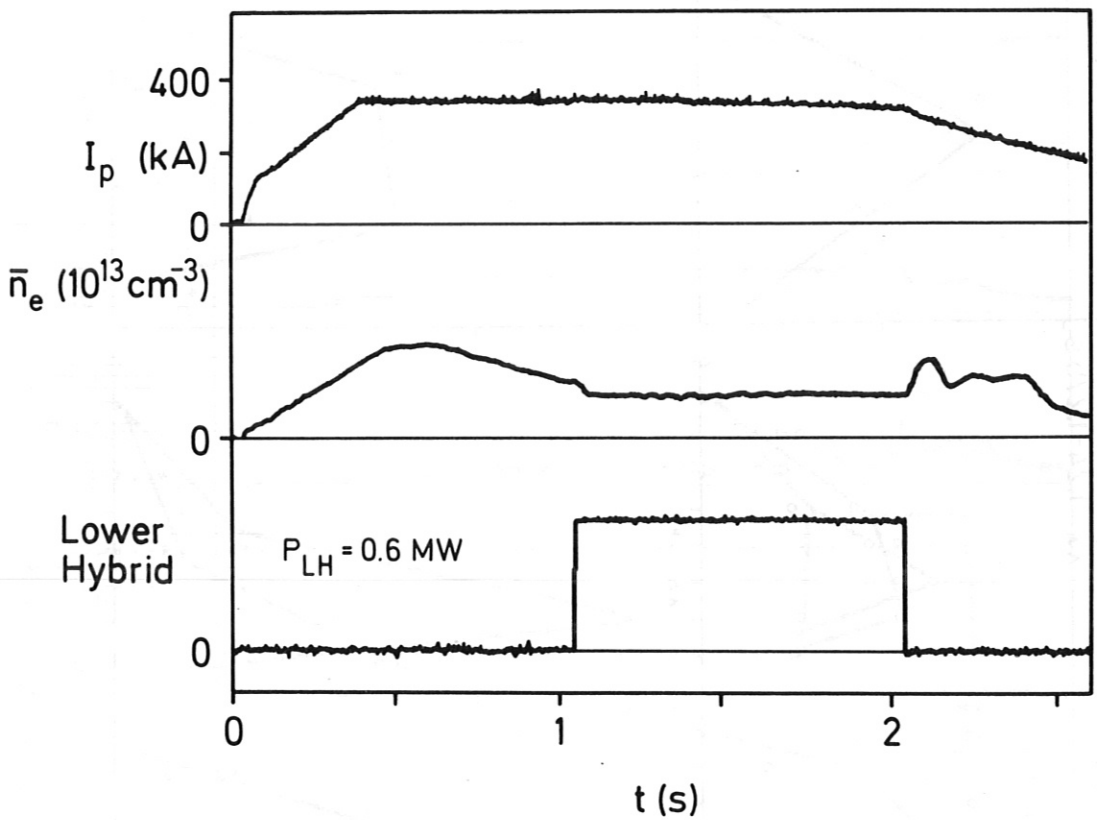

Fig. 28: Plasma current and density during the 'lower hybrid current drive series' #13046-13053.

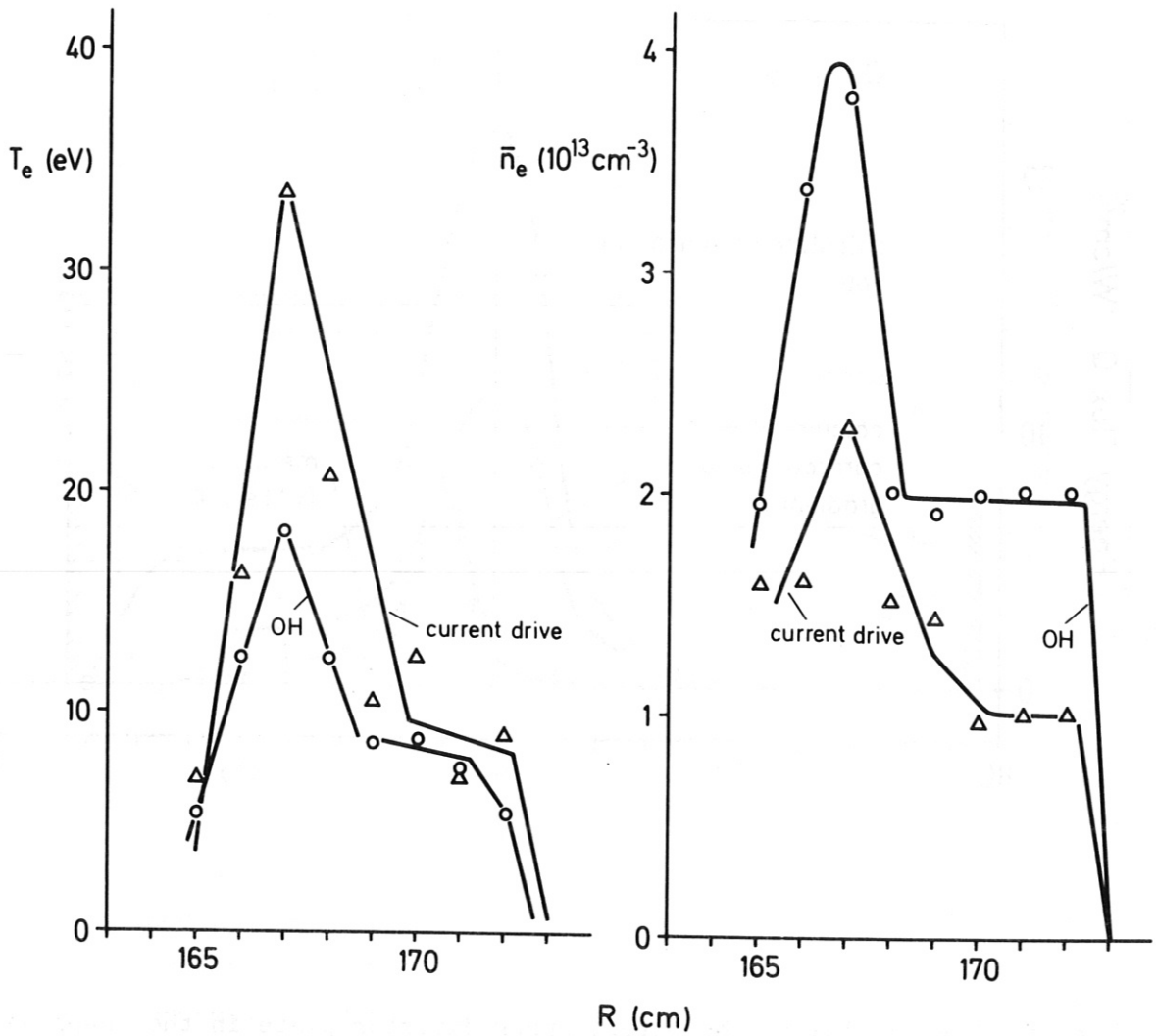

Fig. 29: Profiles in the divertor during the lower hybrid current drive series of discharges.

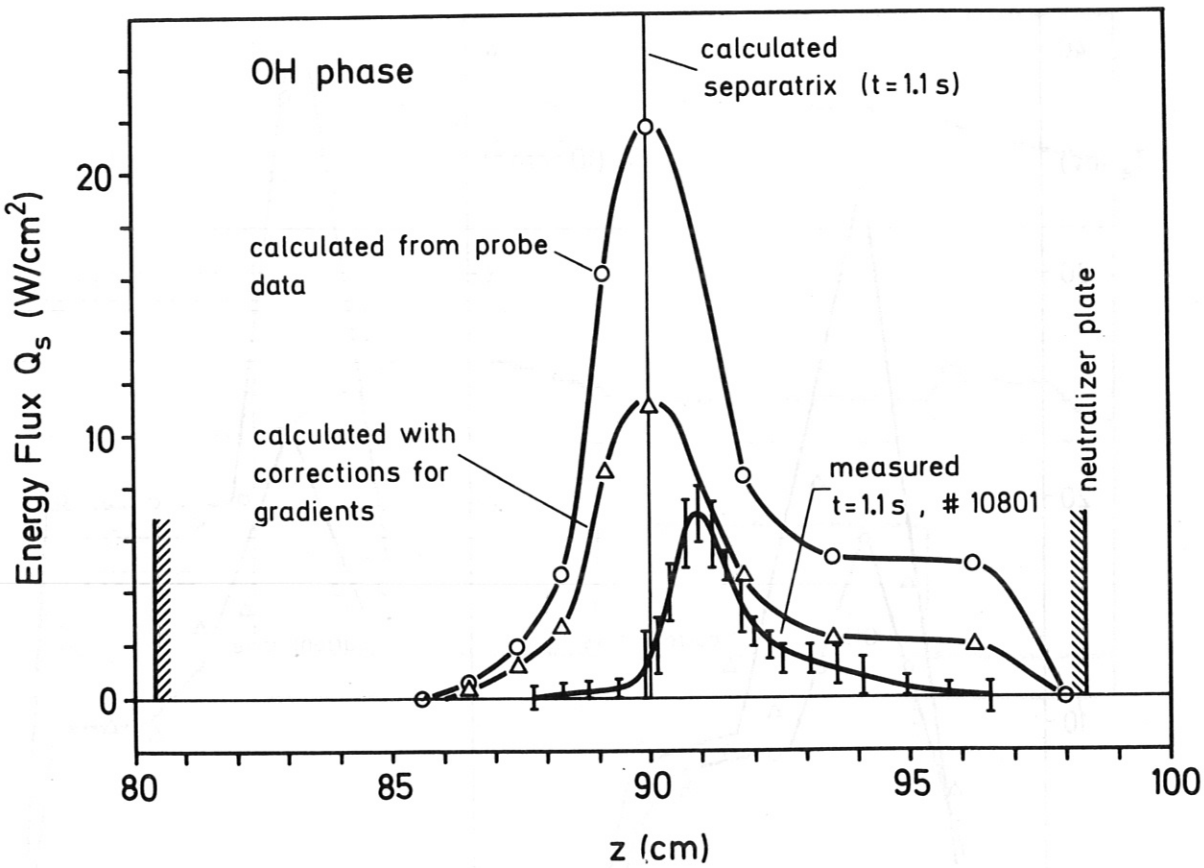

Fig. 30: Energy flux to the outer, upper divertor plate in the OH-phase of discharge #10801 (I_p = 320 kA, $\bar{n}_e$ = 3.6 x 10^{13} cm^{-3}). The theoretical curves are calculated with n_{ed} and T_{ed} from Langmuir probe data. For theoretical curve with corrections for gradients in n_{ed}, T_{ed}, see text.

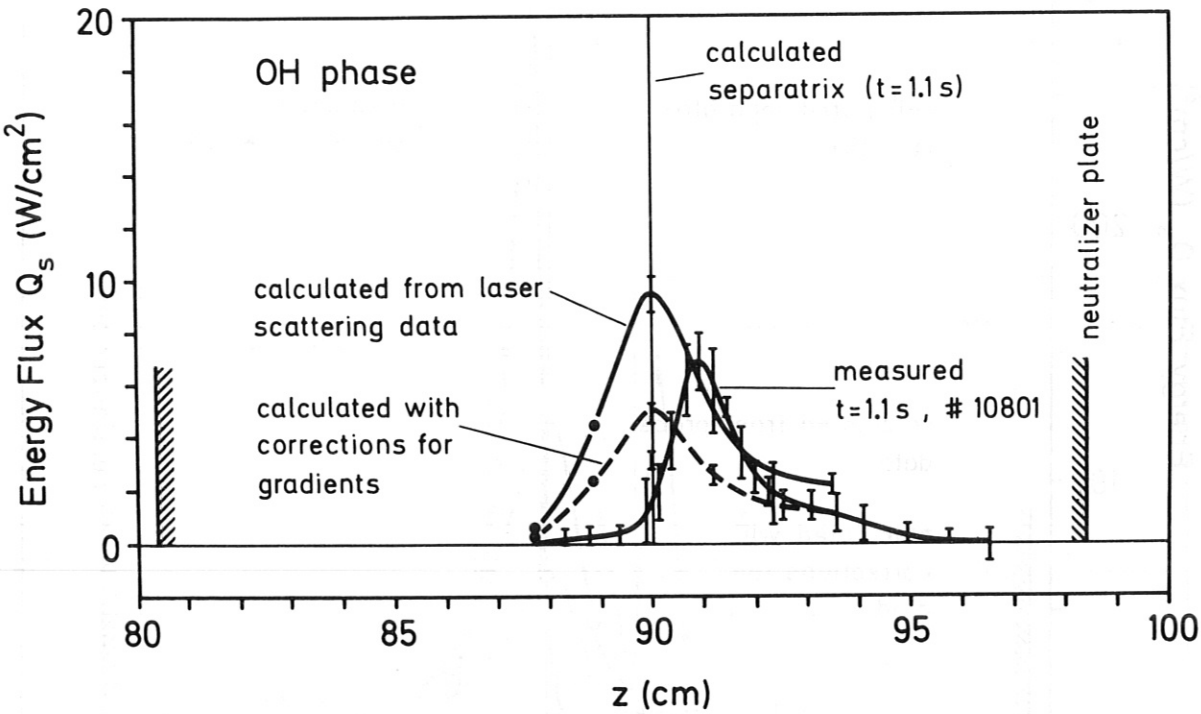

Fig. 31: Energy flux to the outer, upper divertor plate in the OH-phase of discharge #10801 (I_p = 320 kA, $\bar{n}_e$ = 3.6 x 10^{13} cm^{-3}). The theoretical curves are calculated with n_{ed} and T_{ed} from laser scattering data. For theoretical curve with corrections for gradients in n_{ed}, T_{ed}, see text.

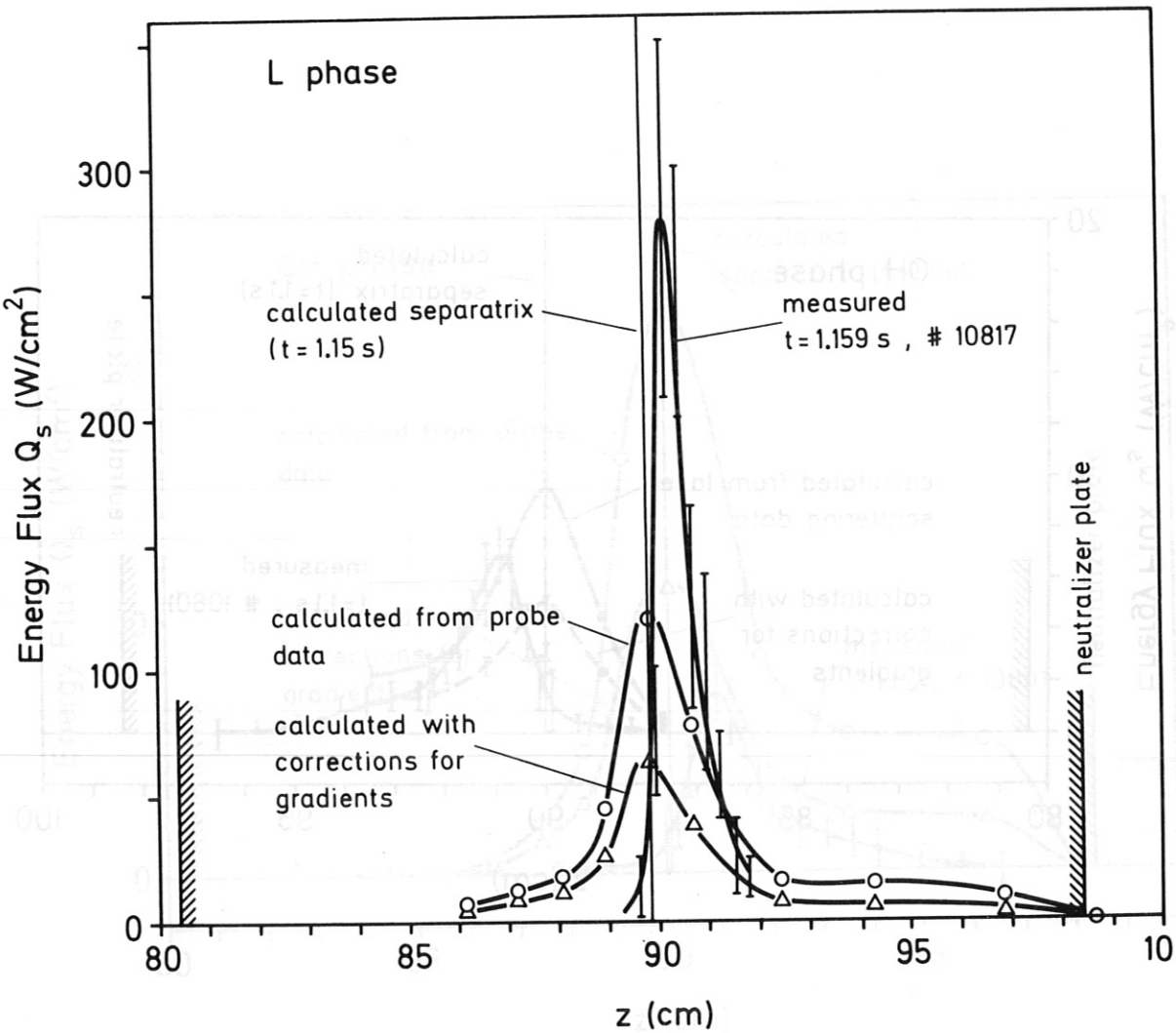

Fig. 32: Energy flux to the outer, upper divertor plate in the L-phase of discharge #10817 (I_p = 320 kA, $\bar{n}_e$ = 3.6 x 10^{13} cm^{-3}). The theoretical curves are calculated with n_{ed} and T_{ed} from Langmuir probe data. For theoretical curve with corrections for gradients in n_{ed}, T_{ed}, see text.

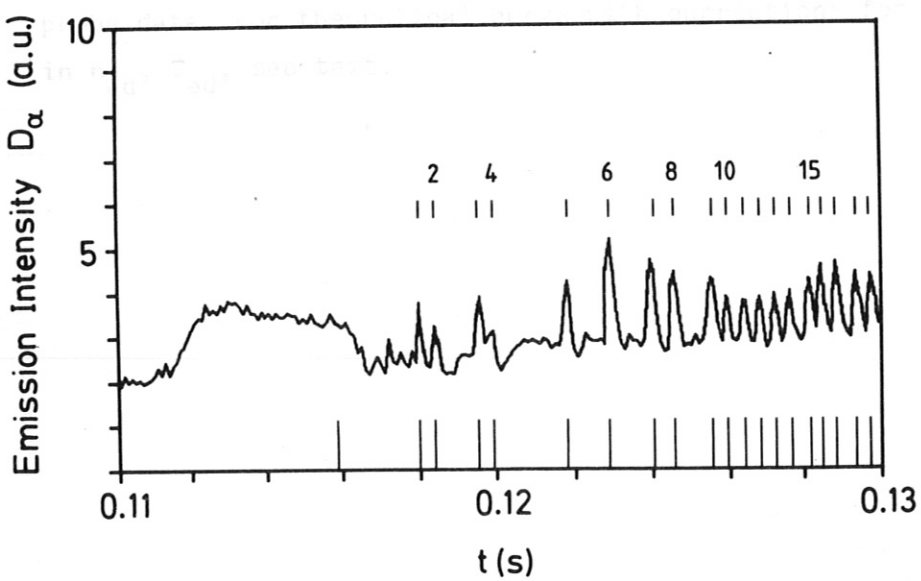

Fig. 33: D_α line emission intensity during the neutral injection phase of discharge # 10817 (I_p = 320 kA, $\bar{n}_e$ = 3.6 x 10^{13} cm^{-3}, P_{NI} = 3.1 MW). The first vertical bar (without number) indicates the time at which the energy flux to the plate in the L-phase (see Fig. 32) was measured. The bars with numbers 1 to 19 indicate bursts in the H-phase. The energy flux to the plate during these bursts is plotted in Fig. 34.

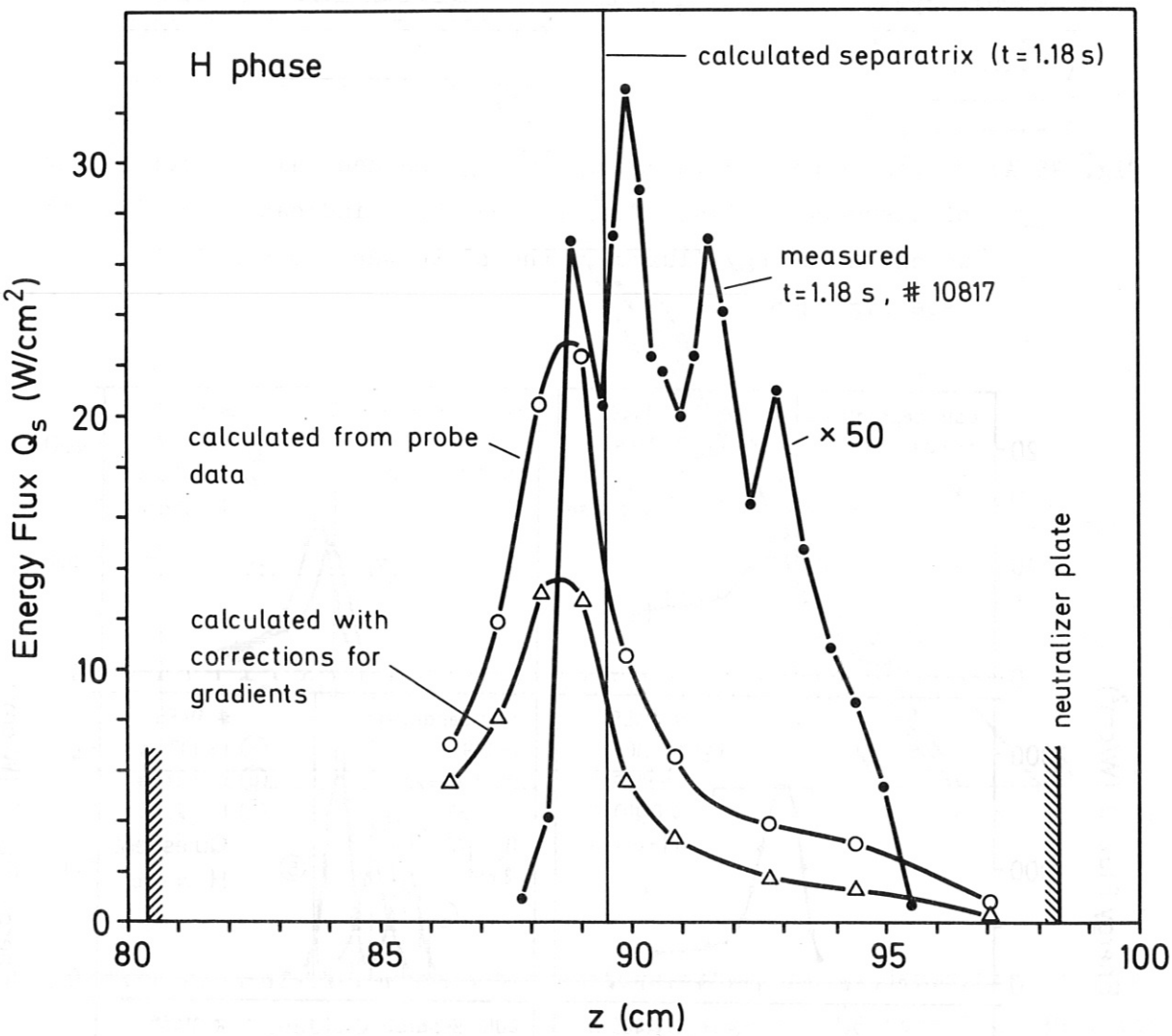

Fig. 34: Energy flux to the outer, upper divertor plate in the H-phase of discharge 10817 (I_p = 320 kA, $\bar{n}_e$ = 3.6 x 10^{13} cm^{-3}, P_{NI} = 3.1 MW). The measured profile is an average of the fluxes during the 19 bursts shown in Fig. 33. The probe data from which the theoretical curves were calculated were taken between bursts. For this particular discharge, the thermographic apparatus did not allow fluxes to be measured in the quiet phases between bursts.

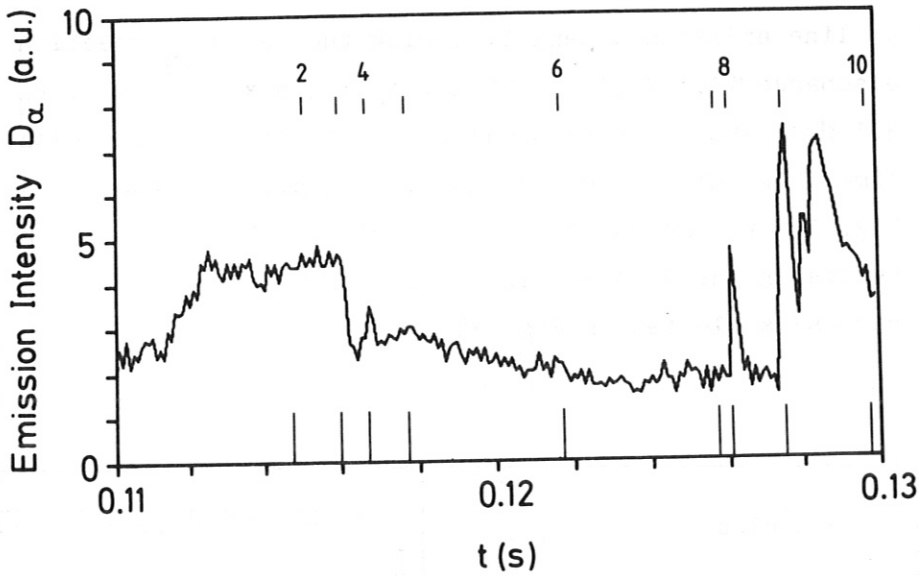

Fig. 35 a: D_α line emission intensity during the neutral injection phase of discharge #11455. The vertical bars indicate the times at which the energy fluxes to the plate were measured (see Fig. 35b).

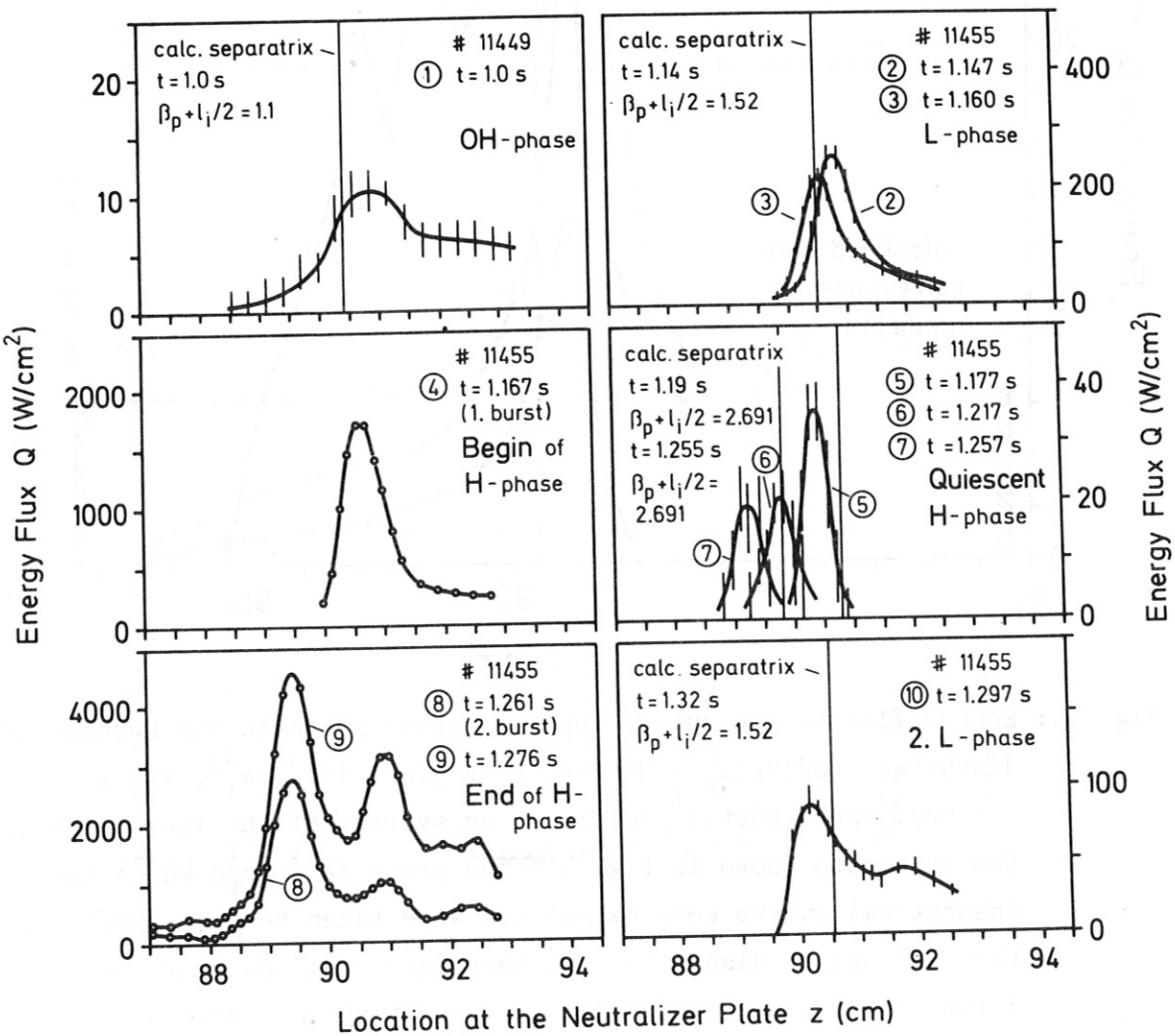

Fig. 35 b: Energy flux to the outer, upper divertor plate in the L and H-phases of discharge #11455. The times at which profiles 2 to 10 were taken are indicated in Fig. 35a.

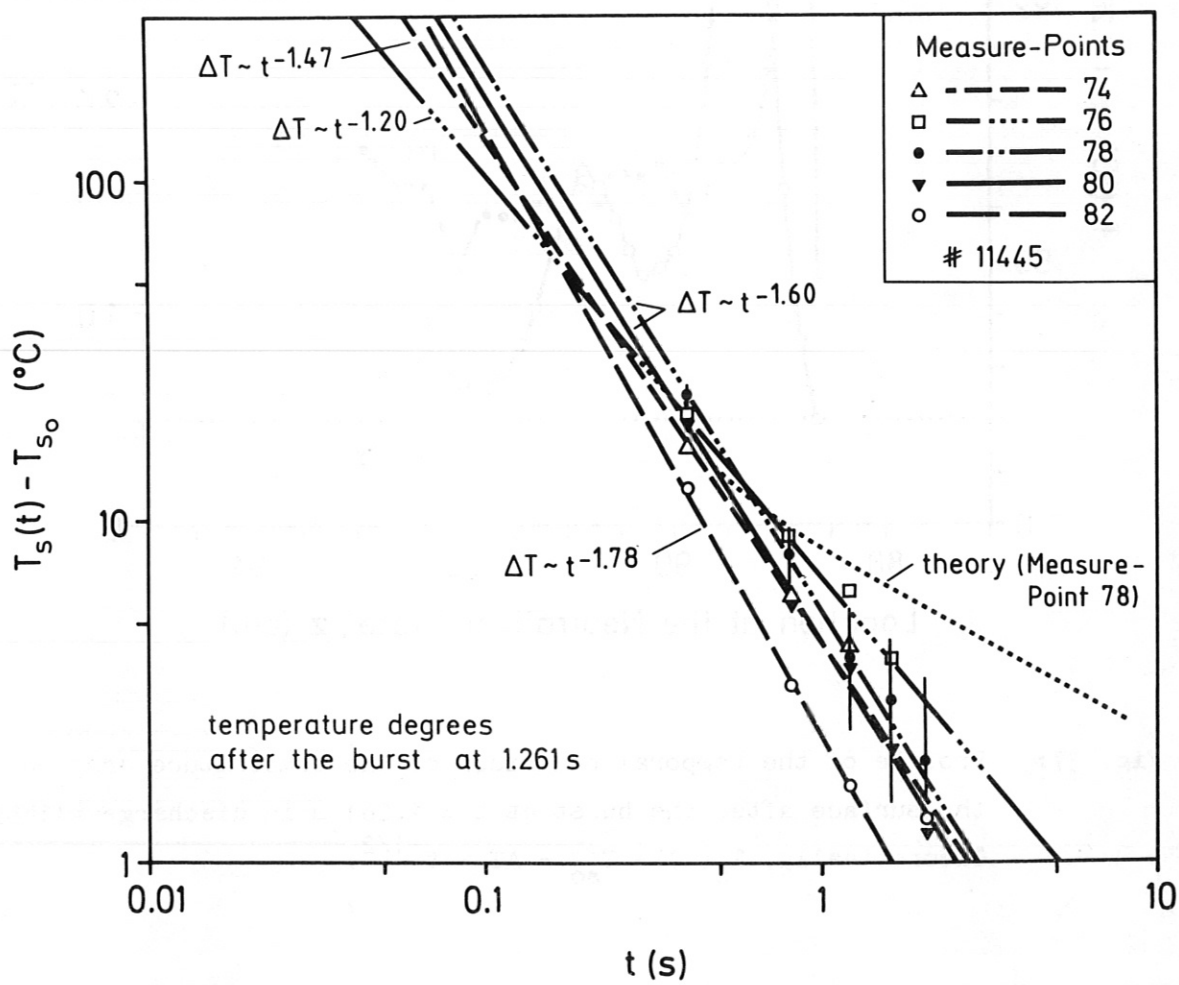

Fig. 36: Drop of the surface temperature after energy deposition during the burst at t = 1.261 s in discharge #11455 (see Fig. 35b) for different measuring points. For theoretical curve, refer to text.

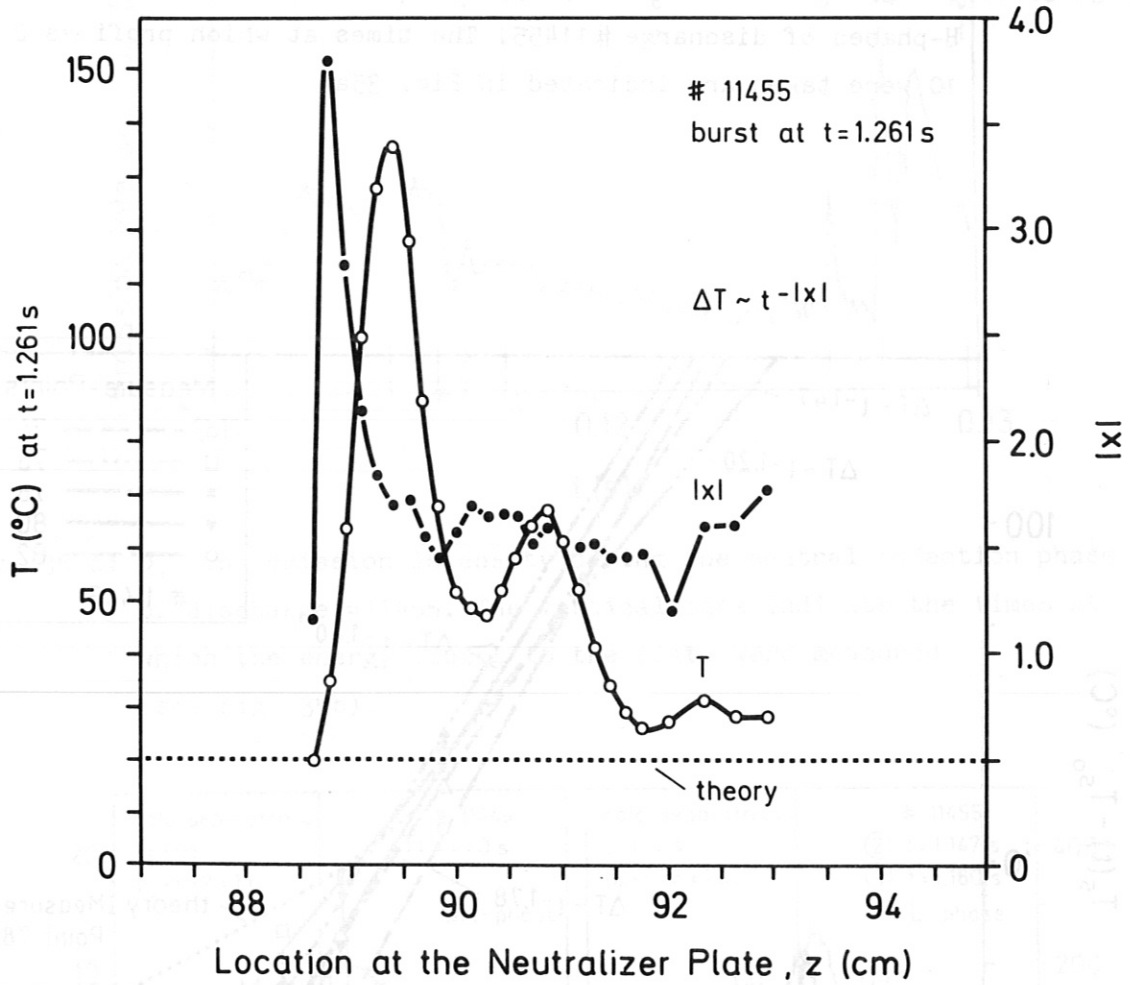

Fig. 37: Profile of the temporal behaviour of the temperature drop on the surface after the burst at t = 1.261 s in discharge #11455. Theoretically, $T_s(t) - T_{so} = \Delta T \sim t^{-1/2}$.